





Cite this: *Soft Matter*, 2025,  
21, 1308

# The effect of selective surface interaction on polymer phase separation with explicit polydispersity during polymerization

Hyeonmin Jeong,<sup>a</sup> Junsu Gu,<sup>b</sup> Paul Mwasame,<sup>b</sup> Kshitish Patankar,<sup>b</sup>  Decai Yu<sup>b</sup>  
and Charles E. Sing  <sup>\*a</sup>

In polymerization-induced phase separation, the impact of polymer–substrate interaction on the dynamics of phase separation for polymer blends is important in determining the final morphology and properties of polymer materials as the surface can act as another driving force for phase separation other than polymerization. We modify the previously-developed polymerizing Cahn–Hilliard (pCH) method by adding a surface potential to model the phase separation behavior of a mixture of two species independently undergoing linear step-growth polymerization in the presence of a surface. In our approach, we explicitly model polydispersity by separately considering different molecular-weight components with their own respective diffusion constants, and with the surface potential preferentially acting on only one species. We first show that the surface potential induces faster phase separation of smaller molecules at early stages before the degree of polymerization becomes large enough to drive bulk phase separation. This model is then used to investigate the degree of anisotropic ordering in a direction perpendicular to the surface over various polymerization rates  $\tilde{k}$  and strengths of the potential  $\tilde{V}$ . We find that at low  $\tilde{k}$ , smaller molecules have sufficient time to diffuse and accumulate at the potential surface, resulting in richer production of heavier polymers at the surface without the need for larger polymers to diffuse on their own toward the surface. Conversely, at high  $\tilde{k}$ , larger polymers first evenly accumulate throughout the system before undergoing phase separation; the concentration wave initiated from the potential surface then propagates into the bulk, resulting in anisotropic phase separation.

Received 11th September 2024,  
Accepted 13th January 2025

DOI: 10.1039/d4sm01077a

[rsc.li/soft-matter-journal](https://rsc.li/soft-matter-journal)

## 1. Introduction

Surface-directed phase separation (SDPS) describes a phenomenon where a surface exhibits preferential attraction to one component over others in a mixture, thereby inducing phase separation. Consequently, SDPS results in the formation of a wetting layer of the favored component proximal to the surface, accompanied by the propagation of anisotropic concentration waves perpendicular to the surface, extending into the bulk.<sup>1–7</sup> SDPS and the effect of surfaces have been extensively studied in experiments<sup>1,2,8–10</sup> as well as in theoretical and computational research,<sup>4–7,10–20</sup> due not only to the important role of surfaces in inducing unique phase separation behaviors and morphologies but also to their diverse range of applications spanning from food,<sup>21</sup> surface-responsive materials,<sup>22</sup> to photovoltaic devices.<sup>23</sup> The presence of a surface can significantly influence the phase separation behavior in polymeric systems, playing a crucial role in determining the morphology and properties of the

resulting material. First, surfaces introduce different energetic interactions compared to the bulk polymer. The nature of these interactions, whether attractive or repulsive, can affect how polymers adsorb, arrange, and move on the surface. The compatibility between the polymer and the surface material can lead to preferential wetting of one component over another, influencing the phase morphology.<sup>1–7,24</sup> Second, the surface can confine the polymer blend to a limited dimension. This confinement can alter the kinetics and thermodynamics of phase separation, often leading to faster phase separation compared to bulk behavior.<sup>25–27</sup> In addition, while polymers in the bulk phase separate isotropically, the symmetry near a surface is broken, leading to anisotropic domain shapes and orientations.<sup>5,6,28</sup> Hence, it is important to understand molecular-level details of the SDPS process as it provides a means to precisely control phase separation pathways, final properties and structures of materials for targeted specific functions.

In comparison to SDPS, polymerization-induced phase separation (PIPS) describes the phenomenon where initially homogeneous components of a polymer blend or solution spontaneously segregate into separate regions or phases due to chemical disparities as molecular weight increases.<sup>29,30</sup> PIPS

<sup>a</sup> Department of Chemical and Biomolecular Engineering, University of Illinois Urbana-Champaign, Urbana, IL, 61801, USA. E-mail: [cesing@illinois.edu](mailto:cesing@illinois.edu)

<sup>b</sup> Dow Chemical Company, Midland, MI, 48667, USA



presents numerous advantages over conventional phase separation methodologies, notably in its capacity to meticulously regulate the morphology of resultant materials. This includes the attainment of cylindrical,<sup>31,32</sup> lamellar,<sup>33–35</sup> and globular structures,<sup>36–38</sup> each achievable through the evolving morphological processes. Such outcomes are dictated by the intricate interplay between polymerization kinetics and phase separation dynamics, thereby determining the final morphology of the system. PIPS manifests across diverse systems, encompassing polymeric blends, solutions, or colloidal suspensions, typically initiated through thermal<sup>39–42</sup> or photochemical means.<sup>43–46</sup> It finds widespread application in the fabrication of polymer-based materials, notably membranes,<sup>47–49</sup> functional coatings,<sup>50,51</sup> and composites (or adhesives).<sup>52–55</sup> In this sense, comprehending the underlying physics of PIPS and exercising control over this phenomenon are pivotal, given their significant implications across a broad spectrum of industrial and technological applications. Furthermore, combining PIPS and SDPS presents two different time scales of phase separation driven by two competing factors, polymerization and surface potential, for more sophisticated control of phase separating systems.

The classical model of phase separation dynamics in polymer blends integrates two key components: the thermodynamic driving force described by the Flory–Huggins<sup>56</sup> theory of polymer mixing, and the macromolecular transport described by the Cahn–Hilliard<sup>57</sup> formalism. The Flory–Huggins theory considers mean-field pairwise interactions between species, characterized by the Flory–Huggins  $\chi$  parameter, which increases with the degree of immiscibility among different components.<sup>56</sup> In symmetric, binary polymer blends with a degree of polymerization  $N$ , the Flory–Huggins theory predicts phase separation above a critical point at  $\chi N = 2$ , resulting in the formation of two phases; it delineates the thermodynamic state and driving force underlying this phase separation phenomenon.<sup>56</sup> In contrast, the Cahn–Hilliard formalism captures the dynamics of phase separation in polymer systems at continuum length scales, offering insight into the non-equilibrium process leading to the phase-separated state. It is frequently applied to investigate phenomena like spinodal decomposition, material diffusion, and microstructure formation in a range of materials; alloys,<sup>58–60</sup> polymers,<sup>61–66</sup> and others.<sup>67,68</sup>

The Cahn–Hilliard formalism is a form of the diffusion equation integrated with a free energy functional, such as the Flory–Huggins mixing free energy, to simulate the temporal evolution of component densities. In polymer systems, the combination of Flory–Huggins and Cahn–Hilliard models has been extensively utilized for modeling both binary<sup>62–64</sup> and ternary<sup>65,66,69</sup> melt blends, in addition to polymer solutions.<sup>70–76</sup> The Cahn–Hilliard approach offers a notable advantage in its ability to explore larger time and length scales compared to particle-based simulations. Moreover, it has been adapted and widely used to accommodate more complex systems, incorporating features such as reactions<sup>64,74,75,77–82</sup> or coupling with other equations such as the Stokes equation.<sup>62,83,84</sup> The Cahn–Hilliard formalism has provided key insights into the phase separation dynamics of polymer blends such as quantifying the evolution of concentration fluctuations into larger inhomogeneities during the

early stages of phase separation in initially homogeneous and isotropic systems.<sup>85–88</sup> It can also capture the late stage of phase separation driven by interfacial interactions including surface tension,<sup>85,89</sup> where its characteristic scaling of size growth of phase separated domains corresponds to  $t^{1/3}$  ( $t$  is time).<sup>85,86,89–91</sup>

The Cahn–Hilliard equation is a robust tool for modeling and comprehending phase separation phenomena, and remains an active research field given its broad applicability and adaptability to accommodate complex physical scenarios.<sup>92,93</sup> This versatility renders it particularly promising for modeling surface-directed phase separation (SDPS) and polymerization-induced phase separation (PIPS). In this study, we elucidate our approach of coupling a multicomponent Cahn–Hilliard model with surface potential which decays away from the surface during the process of linear step-growth polymerization involving two partially immiscible polymer species. By modeling the complete molecular weight distribution of both species, we explore the interplay among polymerization kinetics, surface potential and phase separation dynamics across all polymer lengths. This comprehensive approach explicitly accounts for the varying molecular mobilities and contributions to the mixing free energy inherent in different polymer lengths.

## 2. Methods

In this study, we modify our previously-developed polymerizing Cahn–Hilliard (pCH) model<sup>94</sup> so that it incorporates the effect of surface and the preferential adsorption of one of the polymer species. We investigate a binary system with two different types of species  $\alpha = A, B$ , with a volume fraction  $\phi_\alpha(\mathbf{r}, t)$  that is a function of space  $\mathbf{r}$  and time  $t$ . For a given species  $\alpha$ , this volume fraction can be further divided into components of different molecular weight  $\phi_{\alpha, N_\alpha}(\mathbf{r}, t)$  such that  $\sum_{N_\alpha} \phi_{\alpha, N_\alpha}(\mathbf{r}, t) = \phi_\alpha(\mathbf{r}, t)$  and there is a molecular weight distribution  $w_\alpha(N_\alpha, \mathbf{r}, t) = \phi_{\alpha, N_\alpha}(\mathbf{r}, t) / \phi_\alpha(\mathbf{r}, t)$ . We assume that the monomers of both species  $\alpha$  are bi-functional and polymerize in linear step-growth fashion with a constant reaction rate  $k_\alpha$  independent of molecular-weight.<sup>95</sup> Our numerical simulation scheme evolves  $\phi_{\alpha, N_\alpha}(\mathbf{r}, t)$  over time and space through diffusion and polymerization from an initial state featuring a homogeneous mixture of monomers A and B ( $\phi_{A,1}(\mathbf{r}, 0) = \phi_{B,1}(\mathbf{r}, 0) = 0.5$ ). All simulations are performed on a two-dimensional grid.

### 2.1. Multi-component Cahn–Hilliard equation

The Cahn–Hilliard equation is used to predict the time-evolution of the component concentration fields,  $\phi_{\alpha, N_\alpha}(\mathbf{r}, t) = \phi_i(\mathbf{r}, t)$ , in the context of phase separation for immiscible material blends.<sup>57</sup> Based on the previously-developed model,<sup>94</sup> we write the Cahn–Hilliard equation in a non-dimensional form:

$$\frac{\partial \phi_i(\tilde{\mathbf{r}}, \tilde{t})}{\partial \tilde{t}} = \tilde{\nabla} \cdot \left[ \tilde{M}_{ij}(\tilde{\mathbf{r}}, \tilde{t}) \tilde{\nabla} \left( \frac{\delta \tilde{f}_h(\{\phi_k\})}{\delta \phi_j(\tilde{\mathbf{r}}, \tilde{t})} - \tilde{\kappa} \tilde{\nabla}^2 \phi_j(\tilde{\mathbf{r}}, \tilde{t}) \right) \right] = \mathcal{A}_{\text{CH}}(\tilde{\mathbf{r}}, \tilde{t}) \quad (1)$$

This equation is rendered non-dimensional *via* a reference mobility  $M_0$ , a reference molecular weight  $N_0$ , a reference



distance  $L_0$ , and a reference timescale  $t_0 = L_0^2/M_0$ . In eqn (1), the indices  $i, j$  and  $k$  refer to both the species  $\alpha$  and the specific degree of polymerization  $N_\alpha$  for explicitly treating the polydispersity of each species. The Onsager coefficient  $\tilde{M}_{ij}$  is non-dimensionalized by the reference mobility  $M_0 = k_B T / 6\pi a N_0 \zeta$ ;  $k_B T$ ,  $a$  and  $\zeta$  represent thermal energy, effective hydrodynamic radius, and monomer friction coefficient, respectively. We treat as simply  $\tilde{M}_{ij}(\tilde{\mathbf{r}}, \tilde{t}) = \phi_i(\tilde{\mathbf{r}}, \tilde{t}) M_i \delta_{ij} / M_0 = \phi_i \tilde{M}_i \delta_{ij}$  under the Rouse dynamics assumption that mobility is inversely proportional to molecular weight (*i.e.*  $\sim 1/N_i$ ). Finally, we introduce a shorthand denoting the entire right-hand side of the first equation as  $\mathcal{A}_{\text{CH}}(\tilde{\mathbf{r}}, \tilde{t})$ , which we later use in describing our numerical procedure combining the Cahn–Hilliard formalism with reaction kinetics.

In our approach to modeling the thermodynamics of polymers, in addition to a surface potential  $\tilde{V}(\tilde{\mathbf{r}})$  we will discuss later, we consider a Flory–Huggins contribution to the homogeneous free energy density  $\tilde{f}_{\text{FH}}(\tilde{\mathbf{r}}) = \tilde{f}_{\text{FH}}(\tilde{\mathbf{r}}) + \tilde{V}(\tilde{\mathbf{r}})$  at position  $\tilde{\mathbf{r}}$ .<sup>94</sup>

$$\tilde{f}_{\text{FH}}(\tilde{\mathbf{r}}) = \sum_{N_A=1}^{N_{A,\text{max}}} \left( \frac{\phi_{A,N_A}(\tilde{\mathbf{r}}) \ln \phi_{A,N_A}(\tilde{\mathbf{r}})}{N_A} \right) + \sum_{N_B=1}^{N_{B,\text{max}}} \left( \frac{\phi_{B,N_B}(\tilde{\mathbf{r}}) \ln \phi_{B,N_B}(\tilde{\mathbf{r}})}{N_B} \right) + \chi \phi_A(\tilde{\mathbf{r}}) \phi_B(\tilde{\mathbf{r}}) + \frac{\xi}{2} (\phi_A(\tilde{\mathbf{r}}) + \phi_B(\tilde{\mathbf{r}}) - 1)^2 \quad (2)$$

This expression is normalized by the thermal energy  $k_B T$ .  $N_{A,\text{max}}$  and  $N_{B,\text{max}}$  represent the maximum degrees of polymerization that are chosen for practical considerations, and beyond which polymers are assumed to diffuse similarly slowly,  $\chi$  is the Flory–Huggins interaction parameter, and  $\xi$  is a compressibility parameter. We choose  $\xi = 100$  as a suitably high value to ensure that  $\sum_i \phi_i \approx 1$ , while permitting small local fluctuations in concentration to enhance the numerical stability of our methodology. This deviation from traditional methods of solving the Cahn–Hilliard equation, which typically maintain strict mass conservation by evaluating  $n - 1$  transport equations against a reference component,<sup>71–73,80,88,96</sup> renders our approach more numerically manageable. This adaptation of  $\tilde{f}_{\text{FH}}$  incorporates different degrees of polymerization  $N_A$  or  $N_B$ , treating them as distinct species characterized by their respective density fields,  $\phi_{A,N_A}$  and  $\phi_{B,N_B}$ , which independently contribute to the mixing entropy. Concurrently, the sum over fields A and B (*i.e.*  $\phi_\alpha = \sum_{N_\alpha=1}^{N_{\alpha,\text{max}}} \phi_{\alpha,N_\alpha}$ ) impacts both the enthalpic  $\chi$  term, and the incompressibility constraint.<sup>97</sup>

The gradient energy coefficient  $\tilde{k}$  is treated as a constant based on the Random Phase Approximation<sup>98–101</sup> such that  $\kappa = b^2 / (36 \langle \phi_A \rangle \langle \phi_B \rangle)$  where  $b$  denotes the Kuhn length, and we use the overall volume fractions of the species  $\langle \phi_A \rangle$  and  $\langle \phi_B \rangle$  for simplicity. This form of the square gradient term is notably approximate and independent of chain length; however, more sophisticated treatments would account for  $N_A$  and  $N_B$  that may be non-negligible for short chains and of interest for future studies.<sup>102</sup> We do not expect those to be important for this compressible scheme, where gradients in one species do not

directly imply gradients in the other species, but this may also be of interest for future studies. To keep the length scale consistent with the previous work,<sup>94</sup> we keep  $\tilde{k} = 10$  and a reference molecular weight of  $N_0 = 10$  to define the length scale  $L_0 = C \times R_{G,0}$  as a fraction  $C$  of the radius of gyration of the reference chain. Therefore, the use of a reference chain length to render our equations dimensionless only sets the interfacial length scale *versus* the grid discretization, and not the relationship between chains of different lengths. Similarly, off-diagonal contributions to the square gradient term (*i.e.* relating the gradient of species A to species B) have been shown to be important for incompressible models.<sup>103</sup> Thus,  $C$  depends on the choice of the reference chain length  $N_0$  such that the relationship  $C = [6 \langle \phi_A \rangle \langle \phi_B \rangle \tilde{k} N_0]^{-1/2}$  holds. The temporal and spatial dimensions of our model are constrained by the requirement for an adequately large  $\kappa$  to ensure numerical stability. Considering the typical length scales (*i.e.*  $a \sim 0.5$  nm) and based on prior definitions, we observe that phase separation occurs on the order of *ca.* 10  $\mu\text{s}$  in our system.

For real systems with longer polymers, the relevant time scales would naturally be extended, but our reaction rate constant  $\tilde{k}$  is considerably faster than those typically observed in experimental settings.<sup>95</sup> We anticipate that the physical arguments presented in this paper should scale directly to experimentally relevant time scales.

## 2.2. Surface

The presence of a surface significantly impacts the behavior of phase separation in polymer systems, playing a vital role in shaping the morphology and characteristics of the final material.<sup>1,2,4–20</sup> In our scheme, we implement the Neumann boundary condition at  $\tilde{x} = 1$  and  $\tilde{x} = Z$ , where  $\tilde{x}$  denotes the  $x$ -coordinate of  $\tilde{\mathbf{r}}$ , and  $Z$  represents the number of discretized grids along both  $x$ - and  $y$ -directions, and is set to 64. This approach ensures no flux of polymers across the boundaries, effectively creating impenetrable surfaces at both ends of the  $x$ -axis. Conversely, we employ periodic boundary conditions along the  $y$ -direction.

The Neumann condition at the  $x$ -boundaries can be expressed as:

$$\left. \frac{\partial \mu}{\partial \tilde{x}} \right|_{\tilde{x}=1} = \left. \frac{\partial \mu}{\partial \tilde{x}} \right|_{\tilde{x}=Z} = 0 \quad (3)$$

where  $\mu$  is the chemical potential.

This combination of boundary conditions allows for the simulation of a confined system in the  $x$ -direction while maintaining periodicity in the  $y$ -direction, providing a robust framework for studying polymer dynamics under the presence of a surface.

## 2.3. Surface potential

Surfaces that exhibit energetically favorable interactions with only one species, polymer A, can induce different phase behaviors compared to those observed in the bulk. The characteristics of these interactions, whether attractive or repulsive, influence the adsorption, arrangement, and mobility of polymers on the surface, which may result in the preferential



wetting of one component over another, thereby impacting the overall phase separation dynamics.<sup>1–7,24</sup> For our simulation, we apply the surface potential  $\tilde{V}$  for only one surface at  $\tilde{x} = \theta_s = 1$ , and it exponentially decays away from the surface in the  $x$ -direction as follows:

$$\tilde{V}(\tilde{x}) = \tilde{V}_0 \exp(-\gamma(\tilde{x} - \theta_s)) \quad (4)$$

Here, the surface potential  $\tilde{V}$  is normalized by the thermal energy  $k_B T$ .  $\tilde{V}_0$  is the initial surface potential at the surface ( $\tilde{x} = \theta_s$ ), and  $\gamma$  is the decaying strength of the potential. In this method, we choose  $\gamma = 0.2$ , for which  $\tilde{V}_0$  decays to less than 1 percent of its original value at  $\tilde{x} = 25$ . In other words, the decaying potential spans roughly two-fifths of the simulation box along the  $x$ -direction.

## 2.4. Polymerization kinetics

In our framework, polymers grow through linear step-growth polymerization, adhering to the rate laws for each chemical species  $\alpha$ :

$$\begin{aligned} \frac{d\phi_{\alpha,N_\alpha}(\tilde{\mathbf{r}}, \tilde{t})}{d\tilde{t}} = & \tilde{k} \left[ \sum_{N'_\alpha=1}^{N_\alpha-1} \frac{\phi_{\alpha,N'_\alpha}(\tilde{\mathbf{r}}, \tilde{t}) \phi_{\alpha,N_\alpha-N'_\alpha}(\tilde{\mathbf{r}}, \tilde{t})}{N_\alpha - N'_\alpha} \frac{N_\alpha}{N'_\alpha} \right. \\ & \left. - \sum_{N'_\alpha=1}^{N_{\alpha,\max}-N_\alpha} \frac{\phi_{\alpha,N_\alpha}(\tilde{\mathbf{r}}, \tilde{t}) \phi_{\alpha,N'_\alpha}(\tilde{\mathbf{r}}, \tilde{t})}{N'_\alpha} \right] = \mathcal{A}_P(\tilde{\mathbf{r}}, \tilde{t}) \end{aligned} \quad (5)$$

The terms depicted on the right-hand side of the equation denote generation and consumption, respectively. We again introduce the shorthand  $\mathcal{A}_P$  for this term, to be used to describe our numerical calculation. In eqn (5),  $\tilde{k} = kt_0/(\tilde{v}_0 L_0^3)$  represents the reaction rate, which is normalized using the reference timescale and length scales, and encompasses the dimensionless monomer volume  $\tilde{v}_0$ . The conversion from volume fraction to number densities is achieved by dividing volume fractions of corresponding polymers by  $N_\alpha$  and  $N'_\alpha$ . In our scheme, we impose a restriction on the upper limit of the molecular weight distribution,  $N_{\alpha,\max}$ , which has only minor quantitative effects on our results. For the linear step-growth polymerization, we adhere to the standard assumption that  $\tilde{k}$  remains constant throughout the simulation, independent of molecular weight.<sup>95</sup>

The polymer concentration field evolves over time *via* both diffusion and local extent of polymerization. To account for both of these process, we consider a straightforward combination of both eqn (1) and (5), that sequentially evaluates the change in polymer density at each time  $\tilde{t}$  and location  $\tilde{\mathbf{r}}$ . We write our time-evolution scheme as:

$$\phi_{\alpha,N_\alpha}(\tilde{\mathbf{r}}, \tilde{t} + \Delta\tilde{t}) = \phi_{\alpha,N_\alpha}(\tilde{\mathbf{r}}, \tilde{t}) + \Delta\tilde{t}[\mathcal{A}_{CH}(\tilde{\mathbf{r}}, \tilde{t}) + \mathcal{A}_P(\tilde{\mathbf{r}}, \tilde{t})] \quad (6)$$

In this case, the change in density fields based on the Cahn–Hilliard equation and the polymerization rate laws are independently added to give the overall change in field densities.

In this work, we comprehensively examine the full range of molecular weights, enabling us to explore the entire mass

distribution function  $w_A(N_A, \tilde{t})$  as a function of  $\tilde{t}$ . Furthermore, our model incorporates an assessment of the reaction kinetics associated with step-growth polymerization by monitoring various metrics, including both the number-averaged  $\langle N_A \rangle_n$  and weight-averaged  $\langle N_A \rangle_w$  degree of polymerization of the A-component, as well as the entire distribution function  $w_A(N_A, \tilde{\mathbf{r}}, \tilde{t})$ . Finally, we utilize equal reaction rates for both species (*i.e.*  $\tilde{k}_A = \tilde{k}_B$ , such that the system is symmetric) and data for each set of parameters reported represents an average over 30 independent trajectories.

## 3 Results

With our pCH model, we study polymerization-induced phase separation under the effect of surface potential which decays away from the surface. We consider symmetric blends where both A and B species exhibit the same polymerization rate constant  $\tilde{k}$ , and the only difference is how they are affected by the surface potential  $\tilde{V}$ . This complex process is quantified and characterized by using the degree of phase separation  $\psi(\tilde{t})$ , degree of anisotropy  $E(\tilde{\mathbf{r}}, \tilde{t})$ , overarching order parameter  $\omega(\tilde{x}, \tilde{t})$ , and ordering transition point  $\tilde{x}_{0=0}(\tilde{t})$ . First,  $\psi(\tilde{t})$  is defined as:

$$\psi(\tilde{t}) = 1 - \frac{\langle \phi_A(\tilde{t}) \phi_B(\tilde{t}) \rangle}{\langle \phi_A(\tilde{t}) \rangle \langle \phi_B(\tilde{t}) \rangle} \quad (7)$$

The angle brackets indicate a spatial average. This expression reflects the difference in local volume fractions between two different components, averaging and normalizing over the entire space to yield a number between  $\psi(\tilde{t}) = 0$  and 1. A fully homogeneous system holds the relationship  $\langle \phi_A(\tilde{t}) \phi_B(\tilde{t}) \rangle = \langle \phi_A(\tilde{t}) \rangle \langle \phi_B(\tilde{t}) \rangle$  such that  $\psi(\tilde{t}) = 0$ . In a fully phase-separated system, the values of  $\psi(\tilde{t})$  is nearly 1 since  $\phi_A(\tilde{t})$  or  $\phi_B(\tilde{t})$  is close to zero, making the second term vanish in eqn (7). Thus, a phase separation process will proceed from the  $\psi(\tilde{t})$  value of 0 toward 1 over time; the endpoint is determined by the phase separation intensity and the interface width between the two bulk phases. In addition, we similarly define  $\psi_x(\tilde{x}, \tilde{t})$ :

$$\psi_x(\tilde{x}, \tilde{t}) = 1 - \frac{\langle \phi_A(\tilde{\mathbf{r}}, \tilde{t}) \phi_B(\tilde{\mathbf{r}}, \tilde{t}) \rangle_y}{\langle \phi_A(\tilde{\mathbf{r}}, \tilde{t}) \rangle_y \langle \phi_B(\tilde{\mathbf{r}}, \tilde{t}) \rangle_y} \quad (8)$$

$\psi_x(\tilde{x}, \tilde{t})$  is averaged over only the  $y$ -direction to measure the degree of phase separation in one slice at each fixed  $\tilde{x}$  value, unlike the overall degree of phase separation  $\psi(\tilde{t})$  which is averaged over all space. Fig. 1a exhibits phase separation behavior along the  $x$ -direction from one surface ( $\tilde{x} = 1$ ) to the other ( $\tilde{x} = 60$ ); the time advances from red ( $\tilde{t} = 0$ ) to purple ( $\tilde{t} = \tau_p$ ), where  $\tau_p$  is the phase separation time for the system to reach  $\psi(\tau_p) = 0.4$ . This arbitrary choice for the definition of  $\tau_p$  is a heuristic that we find useful for quantifying the overall kinetics of phase separation, though is not specific to the surface-driven processes that we will consider in more detail later in this article. Fig. 1a plots  $\psi_x(\tilde{x}, \tilde{t})$  *versus*  $\tilde{x}$  for several time points  $\tilde{t}$ , and shows how the phase separation evolves. To be more specific, near  $\tilde{x} = 1$ ,  $\psi_x(\tilde{x}, \tilde{t})$  rises quickly because the surface potential attracts the preferred species type A and induces phase separation, whereas in the “bulk” ( $\tilde{x} = 40$ ), it





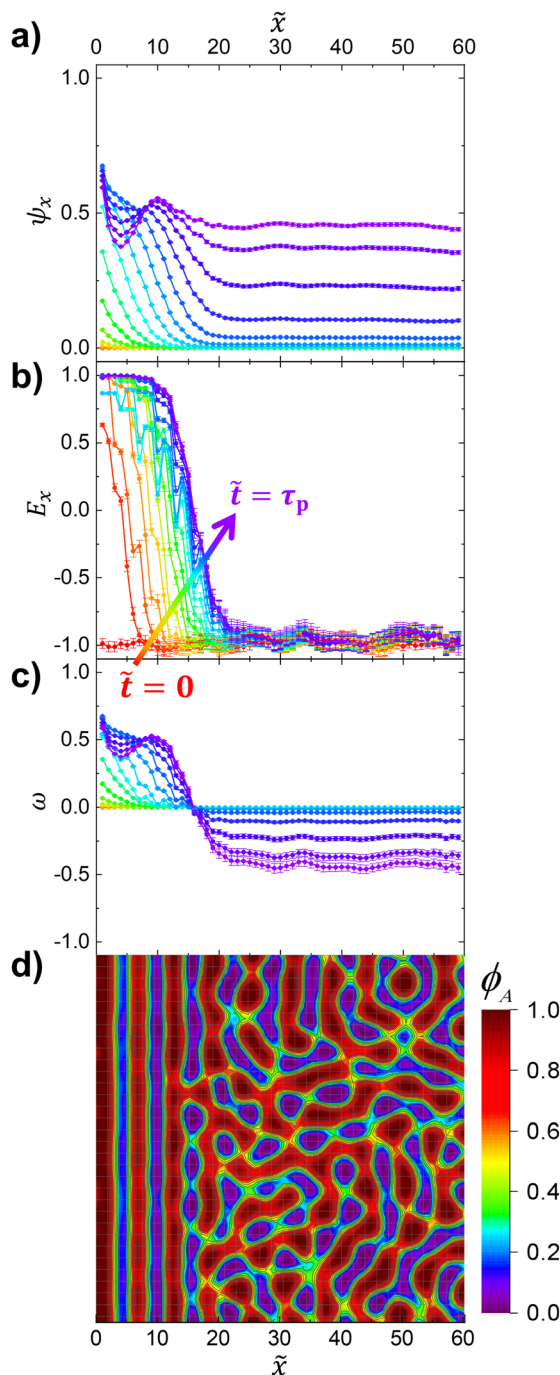


**Fig. 1** Plots illustrating a representative phase separation process, with  $V_0 = 10^{-2}$ ,  $\chi = 0.8$ , and  $\tilde{k} = 10^{-2}$ . All figures share the same  $\tilde{x}$ -axis as the simulation box; (a) to (c) use color scale from red ( $\tilde{t} = 0$ ) to purple ( $\tilde{t} = \tau_p$ ), and the color scale in (d) represents  $\phi_A$  from 0 (purple) to 1 (red). (a) The degree of phase separation  $\psi_x(\tilde{x}, \tilde{t})$ , where 0 and 1 indicate well-mixed and fully phase-separated states, respectively. It represents earlier phase separation near the surface potential ( $\tilde{x} = 1$ ), and late occurrence of phase separation around  $\tilde{x} = 40$ , which we define as the “bulk” regime. (b) The degree of anisotropy  $E_x(\tilde{x}, \tilde{t})$ , which scales from 1 to  $-1$  for anisotropic and isotropic structures, respectively. It shows that an initially isotropic system develops an anisotropic structure near the surface potential ( $\tilde{x} = 1$ ) and isotropic phase separation in the bulk ( $\tilde{x} = 40$ ). (c) Order parameter  $\omega(\tilde{x}, \tilde{t})$  shows directional phase separation; 1,  $-1$  and 0 denote anisotropic, isotropic and no phase separation, respectively. Anisotropic phase separation takes place near the surface potential ( $\tilde{x} = 1$ ) and isotropic phase separation in the bulk ( $\tilde{x} = 40$ ). (d) Snapshot of the concentration profile showing surface-directed spinodal decomposition at  $\tilde{t} = \tau_p$ , where phase separation with directionality is shown.

phase separates based on polymerization rather than surface potential due to its exponential decay. The strength of phase separation  $\psi_x(\tilde{x}, \tilde{t})$  is weaker at  $\tilde{x} = 40$  than  $\tilde{x} = 1$ , which we attribute to the decay of the surface potential. At  $\tilde{x} = 40$ , the system effectively reproduces the bulk phase separation behavior unaffected by the surface potential. The smooth fluctuation in  $\psi_x(\tilde{x}, \tilde{t} = \tau_p)$  near the surface potential ( $\tilde{x} < 20$ ) is due to the presence of alternating interfaces between lamellar-like stripes, where eqn (8) outputs quantities close to 0 for  $\psi_x(\tilde{x}, \tilde{t})$  at interfaces (e.g.  $\langle \phi_A(\tilde{\mathbf{r}}, \tilde{t}) \rangle_y = 0.5$ ) and are not considered “phase separated” with this metric. Eqn (8) thus does not distinguish a locally well-mixed regime from the interface between phase separated domains, because their  $\langle \phi_A(\tilde{\mathbf{r}}, \tilde{t}) \rangle$  values are the same. Although  $\psi_x(\tilde{x}, \tilde{t})$  is a useful parameter to measure the degree of phase separation, it does not quantify the anisotropic ordering behavior arising from the surface potential.

To measure the extent to which phase separation driven by the surface potential produces an anisotropic concentration wave perpendicular to the surface and quantify this anisotropic ordering behavior, we introduce a value that quantifies the degree of anisotropy  $E_x(\tilde{x}, \tilde{t})$ :<sup>104</sup>

$$E_x(\tilde{x}, \tilde{t}) = 4 \frac{\langle v_x^2(\tilde{\mathbf{r}}, \tilde{t}) \rangle_y}{\langle v_x^2(\tilde{\mathbf{r}}, \tilde{t}) + v_y^2(\tilde{\mathbf{r}}, \tilde{t}) \rangle_y} - 3. \quad (9)$$

Here,  $v_x(\tilde{\mathbf{r}}, \tilde{t}) = \frac{d\phi(\tilde{\mathbf{r}}, \tilde{t})}{d\tilde{\mathbf{r}}} \cdot \mathbf{u}_x$  and  $v_y(\tilde{\mathbf{r}}, \tilde{t}) = \frac{d\phi(\tilde{\mathbf{r}}, \tilde{t})}{d\tilde{\mathbf{r}}} \cdot \mathbf{u}_y$ , where  $\mathbf{u}_x$  and  $\mathbf{u}_y$  are the unit vectors in the  $x$ - and  $y$ -direction, respectively.  $E_x(\tilde{x}, \tilde{t})$  ranges from  $-1$  to  $1$  for isotropic and anisotropic ordering structures, respectively, along the direction perpendicular to the potential surface; it is averaged over  $y$ -direction similar to  $\psi_x(\tilde{x}, \tilde{t})$ . Fig. 1b illustrates  $E_x(\tilde{x}, \tilde{t})$  for multiple representative simulation times  $\tilde{t}$ , depicting the progressive ordering behavior extending from the surface potential ( $\tilde{x} = 1$ ) into the bulk towards the other surface ( $\tilde{x} = 60$ ) over time. We find that there is a big jump from the initial time in Fig. 1b reflecting the weak initial ordering behavior induced by the surface potential at  $\tilde{x} = 1$  whereas the regime near the surface on the other side ( $\tilde{x} = 60$ ) does not show anisotropic ordering behavior. However, Fig. 1b alone does not provide any information about the intensity of phase separation. In order to convey the details of both order parameters  $\psi_x(\tilde{x}, \tilde{t})$  and  $E_x(\tilde{x}, \tilde{t})$ , and quantify directional phase separation caused by the surface potential, we introduce an overarching order parameter  $\omega(\tilde{x}, \tilde{t})$  as follows:

$$\omega(\tilde{x}, \tilde{t}) = E_x(\tilde{x}, \tilde{t}) \times \psi_x(\tilde{x}, \tilde{t}). \quad (10)$$

$\omega(\tilde{x}, \tilde{t})$  is introduced to capture both the phase separation and the anisotropic structure;  $\omega(\tilde{x}, \tilde{t})$  at  $-1$ ,  $0$  and  $1$  indicates isotropic full phase separation, no phase separation, and anisotropic full phase separation, respectively. Fig. 1c shows significant anisotropic phase separation near the surface potential at  $\tilde{x} \approx 5$  as indicated by an increasing  $\omega(\tilde{x}, \tilde{t})$ , while isotropic phase separation in the bulk is found near  $\tilde{x} = 40$  as indicated by the negative growth of  $\omega(\tilde{x}, \tilde{t})$ . This is consistent with the corresponding concentration profiles exhibiting the behavior of surface-directed spinodal decomposition near the



surface potential ( $\tilde{x} = 1$ ) shown in Fig. 1d. We note that a surface excess of A could also lead to a positive value of  $\omega(\tilde{x}, \tilde{t})$ , though all  $\chi \neq 0$  cases considered in this manuscript are at values of  $\chi N$  that quickly exceed the critical  $(\chi N)_{\text{crit}} = 2.0$  where symmetric binary blends will spontaneously phase separate. This approach allows us to consider the interplay between surface potential and polymerization, which gets more complex as phase separation is competitively driven by both the surface potential and polymerization.  $\omega(\tilde{x}, \tilde{t}) = 0$  near the potential surface also allows us to characterize the ordering transition point,  $\tilde{x}_{\omega=0}(\tilde{t})$ , at which bulk (isotropic) and lamellar-like (anisotropic) phase separation regimes intersect ( $\tilde{x} \approx 15$ ) as shown in Fig. 1c and d. Measuring  $\tilde{x}_{\omega=0}(\tilde{t})$  provides insight into the effective potential range at which the concentration wave, induced by the potential surface, predominantly decays. This measurement also offers information about the isotropic–anisotropic transition in the system as shown in Fig. 1d.

The consideration of quantities  $\psi_x(\tilde{x}, \tilde{t})$ ,  $E_x(\tilde{x}, \tilde{t})$ ,  $\omega(\tilde{x}, \tilde{t})$ , and  $\tilde{x}_{\omega=0}(\tilde{t})$  enables us to elucidate the interconnected roles of the Flory–Huggins interaction parameter, the reaction rate, and the surface potential in determining their impacts on the phase separation behavior under polymerization and selective surface.

### 3.1. Effect of surface potential strength $\tilde{V}_0$

We first consider how the surface potential strength affects the degree of phase separation  $\psi(\tilde{t})$ , and the effective potential range  $\tilde{x}_{\omega=0}(\tilde{t})$  over time. Here, we keep other parameters such as  $\chi$  and  $\tilde{k}$  the same to isolate the effect of the potential strength.

Starting with the effect of the potential strength on phase separation time, we plot the time-evolution of  $\psi(\tilde{t})$  for various  $\tilde{V}_0$  values including no potential case ( $\tilde{V}_0 = 0$ ) in Fig. 2a. In the case of  $\tilde{V}_0 = 0$ , the phase separation is purely driven by the polymerization which increases the free energetic penalty for longer polymers to remain mixed. For sufficiently long polymer chains, a large value of  $\chi N$  leads to spontaneous phase separation. However, in a system with surface potential, not only the polymerization but also the surface potential plays a role as the driving force for phase separation, suggesting a competition between the two driving forces. In Fig. 2a, as  $\tilde{V}_0$  increases, phase separation occurs at earlier times  $\tilde{t}$ , indicating the higher potential strength drives enhanced molecular transport towards the surface by preferentially attracting one species and prompting an earlier rise of  $\psi(\tilde{t})$ . We note that, in the absence of a driving force for phase separation (*i.e.*  $\chi N = 0.0$ ),  $\psi \sim \mathcal{O}(10^{-3})$  remains very small and there is only a slight increase in the A species at the surface.

Then, we further investigate how anisotropic phase separation emerges in the  $x$ -direction at a specific time  $\tilde{t} = 10 \times 10^5$  denoted by the black dashed line in Fig. 2a. At  $\tilde{t} = 10 \times 10^5$ , we plot  $\omega(\tilde{x})$  in Fig. 2b;  $\omega(\tilde{x}) > 0$  represents anisotropic lamellar-like phase separation in the direction perpendicular to the potential surface, and  $\omega(\tilde{x}) < 0$  indicates isotropic phase separation with no specific directionality. For the zero-potential case ( $\tilde{V}_0 = 0$ ) in Fig. 2b, the system exhibits purely

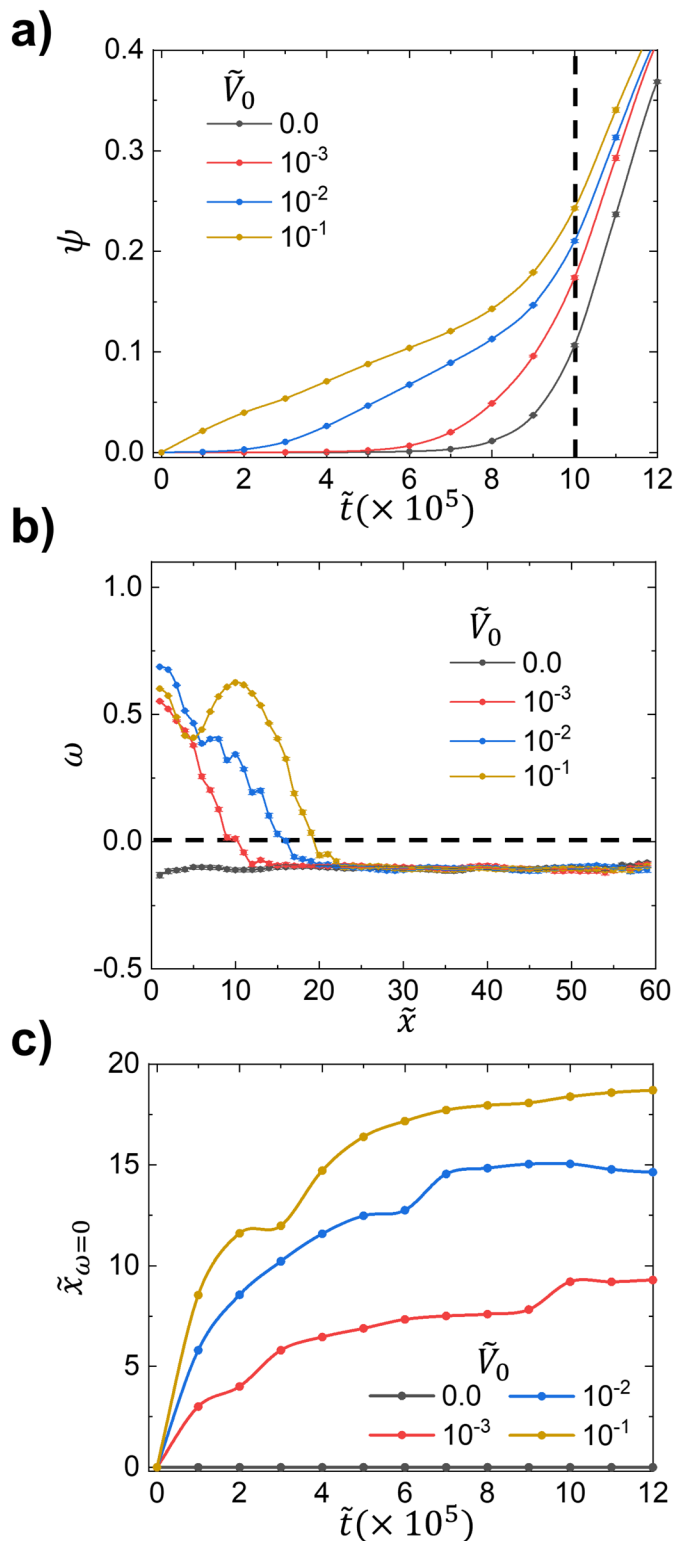


Fig. 2 (a)  $\psi(\tilde{t})$  over different  $\tilde{V}_0$  at constant  $\chi = 0.8$  and  $\tilde{k} = 10^{-3}$ . Phase separation starts earlier as  $\tilde{V}_0$  increases. (b)  $\omega(\tilde{x}, \tilde{t})$  at a specific time  $\tilde{t} = 10 \times 10^5$  from Fig. 2a. For  $\tilde{V}_0 = 0$ , only isotropic phase separation occurs whereas systems with surface potential produces anisotropic phase separation closer to surface potential ( $\tilde{x} = 1$ ). (c) Higher  $\tilde{V}_0$  increases the anisotropic–isotropic transition front  $\tilde{x}_{\omega=0}(\tilde{t})$  (*i.e.* larger anisotropic regime near the surface potential), which gradually increases over time as the concentration wave propagates further into the bulk.



isotropic phase separation ( $\omega(\tilde{x}) < 0$ ), whereas systems with the potential  $\tilde{V}_0 > 0$  show strong alignment ( $\omega(\tilde{x}) > 0$ ) near the potential surface ( $\tilde{x} = 1$ ). In this case,  $\omega(\tilde{x})$  gradually decreases below zero away from the potential surface, entering the “bulk” regime where the system phase separates isotropically. Moreover, the strength of the potential does not affect the intensity of  $\omega(\tilde{x})$  in the bulk regime ( $\tilde{x} \sim 40$ ) as shown in Fig. 2b.

Lastly, we characterize the thickness of the anisotropic regime by the quantity  $\tilde{x}_{\omega=0}(\tilde{t})$  for different  $\tilde{V}_0$  values to examine the extent of surface-guided phase separation over time;  $\tilde{x}_{\omega=0}(\tilde{t})$  describes when  $\omega(\tilde{x}) = 0$  (i.e. intersects with the black dashed line in Fig. 2b). Fig. 2c shows the time-evolution of  $\tilde{x}_{\omega=0}(\tilde{t})$ , demonstrating that stronger  $\tilde{V}_0$  initially produces a thicker anisotropic regime, and the subsequent growth with time is similar such that this initial offset persists regardless of the  $\tilde{V}_0$  values.

### 3.2. Effect of polymer incompatibility $\chi$

We now consider how the Flory–Huggins parameter  $\chi$  governing the polymer incompatibility changes the degree of phase separation  $\psi(\tilde{t})$ , and possibly competes with surface potential as the driving force for phase separation.

To investigate the effect of polymer incompatibility on phase separation under the surface potential, we plot the time evolution of  $\psi(\tilde{t})$  for three representative values of  $\chi$  in Fig. 3. First, we show that larger  $\chi$  values promote faster phase separation regardless of surface potential  $\tilde{V}_0$  at a constant reaction rate  $\tilde{k}$ . In terms of  $\tilde{V}_0$  at each  $\chi$ , we observe a similar trend of  $\psi(\tilde{t})$  with increasing  $\tilde{V}_0$  relative to its corresponding zero-potential system ( $\tilde{V}_0 = 0$ ). For a surface potential of  $\tilde{V}_0 = 10^{-3}$ , the phase separation begins slightly earlier, as indicated by the earlier rise in  $\psi(\tilde{t})$ . As  $\tilde{V}_0$  increases gradually from 0 to  $10^{-1}$ , the influence of the surface potential becomes more pronounced. This enhances anisotropic phase separation (or wetting) behavior, leading to faster phase separation. Interestingly, the impact of  $\tilde{V}_0$  is more significant for systems with lower  $\chi$ . In these systems, weaker polymer incompatibility delays the phase separation because sufficient polymerization and the formation of larger chains are required to drive phase separation. This extended timescale allows the surface potential to attract more components, amplifying its effect on phase separation.

### 3.3. Effect of reaction rate $\tilde{k}$

Fig. 4 is the compilation of the order parameter  $\omega(\tilde{x}, \tilde{t})$  for wide ranges of  $\tilde{k}$  and  $\tilde{V}_0$  values at fixed  $\chi$  of 1.0. In Fig. 4, each row and column shares the same  $\tilde{V}_0$  and  $\tilde{k}$ , respectively. The rainbow color gradient represents the progression of time, transitioning from red ( $\tilde{t} = 0$ ) to purple ( $\tilde{t} = \tau_p$ ), where  $\tau_p$  is defined to characterize the phase separation time at  $\psi(\tilde{t}) = 0.4$ .

First, in Fig. 4, we find that the evolution from the initial profile ( $\tilde{t} = 0$ ) to the subsequent one is higher for larger  $\tilde{V}_0$ . In other words, larger  $\tilde{V}_0$  initially induces stronger accumulation of the preferred species,  $\phi_A$ , at the potential surface  $\tilde{x} = 1$  (i.e. faster growth of  $\omega(\tilde{x}, \tilde{t})$  near  $\tilde{x} = 1$ ) regardless of the reaction rate. This stronger attraction of  $\phi_A$  from a higher surface potential  $\tilde{V}_0$  leads to faster transport and phase separation, and thus smaller  $\tau_p$  as shown in Fig. 2a and 5, respectively.

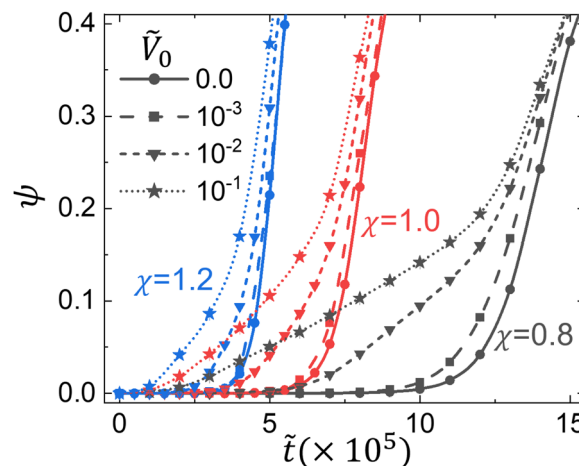


Fig. 3 The influence of the Flory–Huggins parameter,  $\chi$ , which governs polymer immiscibility, on the degree of phase separation  $\psi(\tilde{t})$  at a constant value of  $\tilde{k} = 10^{-2}$ . Each value of  $\chi$  is represented by a distinct color, while different line styles indicate various surface potential  $\tilde{V}_0$ . An increase in  $\chi$  facilitates faster phase separation regardless of surface potential. For each value of  $\chi$ , the effect of  $\tilde{V}_0$  on the progression of phase separation is consistent; a higher surface potential leads to an earlier rise in  $\psi(\tilde{t})$ .

The analysis of varying reaction rates  $\tilde{k}$  in Fig. 4 reveals several key trends. As  $\tilde{k}$  decreases, the generation of larger chains capable of driving phase separation slows down. This results in reduced intensity for  $\omega(\tilde{x}, \tilde{t}) < 0$  near  $\tilde{x} = 40$  at  $\tilde{t} = \tau_p$ . At sufficiently low  $\tilde{k}$  values, surface potential-driven phase separation becomes the dominant mechanism before  $\tilde{t} = \tau_p$ , as evidenced in Fig. 4e, i and m. Notably, systems with surface potential ( $\tilde{V}_0 > 0$ ) at  $\tilde{k} = 10^{-5}$  predominantly display  $\omega(\tilde{x}, \tilde{t}) \geq 0$  for all  $\tilde{x}$  and  $\tilde{t}$ , indicating no isotropic phase separation prior to  $\tau_p$ . In contrast, increasing  $\tilde{k}$  leads to rapid formation of larger polymers, resulting in a decrease in mobility and reduced polymer attraction to the surface potential as shown in Fig. 4. Moreover, Fig. 4k shows a unique behavior; the system at  $\tilde{t} = \tau_p$  (purple) shows contraction near the surface potential instead of further expansion toward the bulk (i.e. reduction of  $\tilde{x}_{\omega=0}(\tilde{t})$ ). This indicates merging of two thin layers of the lamellar-like domain into one thicker layer.

In Fig. 5, to compare each  $\tau_p$  which corresponds to the last purple curve of each sub-figure in Fig. 4, we plot  $\tau_p$  for various combinations of  $\tilde{k}$  and  $\tilde{V}_0$  along with the zero-potential case ( $\tilde{V}_0 = 0$ ). The observed trends across the parameter space are consistent for both diffusion-limited and reaction-limited regimes. For  $\tilde{k} > 10^{-4}$ , the system exhibits diffusion-limited behavior, as shown in Fig. 5. In this regime, increasing the reaction rate  $\tilde{k}$  leads to a longer characteristic phase separation time,  $\tau_p$ . We attribute this phenomena to the rapid accumulation of larger polymer chains with higher  $N_A$ , which significantly slows down molecular diffusion ( $\propto 1/N$ ). Here, the influence of the surface potential  $\tilde{V}_0$  remains consistent across different  $\tilde{k}$  values, but the changes in  $\tau_p$  are minimal. This is expected because, in a diffusion-limited regime, molecular diffusion driven by the surface potential is also restricted and cannot effectively attract long, less-mobile polymers. Conversely, in a reaction-limited regime





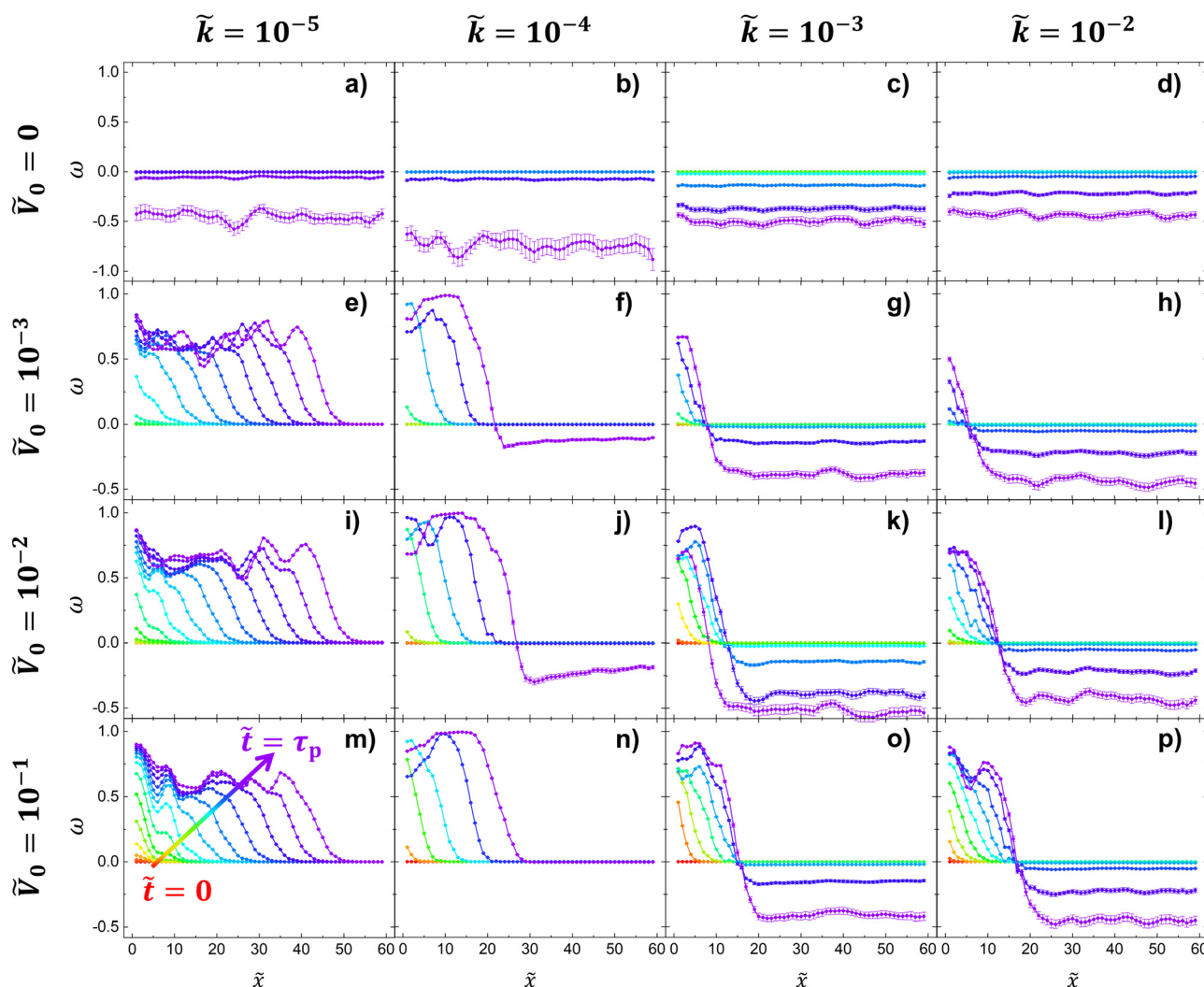


**Fig. 4** The compilation of  $\omega(\tilde{x}, \tilde{t})$  under different conditions of  $\tilde{V}_0$  and  $\tilde{k}$  at constant  $\chi = 1.0$ . Each row and column shares the same  $\tilde{V}_0$  and  $\tilde{k}$ , respectively. For all 16 sub-Fig. 4a–p, the rainbow color gradient represents the progression of time, transitioning from red ( $\tilde{t} = 0$ ) to purple ( $\tilde{t} = \tau_p$ ) denoted with an arrow in Fig. 4m. For the zero-potential systems shown in (a) to (d), systems only isotopically phase separate ( $\omega(\tilde{x}, \tilde{t}) < 0$ ) due to the absence of surface potential. With the surface potential shown in (e) to (p), systems develop positive values of  $\omega(\tilde{x}, \tilde{t})$  near the surface potential ( $\tilde{x} = 1$ ); the spatiotemporal evolution of  $\omega(\tilde{x}, \tilde{t})$  from red ( $\tilde{t} = 0$ ) to next lighter red appears more clearly regardless of  $\tilde{k}$ . At a reaction rate of  $\tilde{k} = 10^{-5}$  in (e), (i) and (m), anisotropic phase separation dominantly propagates and induces ordering behavior ( $\omega(\tilde{x}, \tilde{t}) > 0$ ) throughout the system. Such enhanced penetration is attributed to the prevalent smaller molecules with higher mobility at lower reaction rate  $\tilde{k} = 10^{-5}$ . Furthermore, the difference in timescales between surface-directed and polymerization-induced phase separation plays a pivotal role; the system rapidly reaches  $\tau_p$  due to surface-driven phase separation before polymerization-induced phase separation occurs. When increasing  $\tilde{k}$ , a weaker “wetting” behavior occurs near the surface potential. This phenomena is due to rapid emergence of larger chains with low mobility and rapid consumption of smaller molecules at higher  $\tilde{k}$ . In this regard, at lower  $\tilde{k}$  values, the extended lifetime of smaller chains enhances polymer diffusion under the influence of surface potential.

( $\tilde{k} \lesssim 10^{-4}$ ), the phase separation time  $\tau_p$  decreases with increasing  $\tilde{k}$ . In this scenario, the driving force from polymer incompatibility rapidly intensifies with higher  $\tilde{k}$ , enhancing the rate of phase separation. Unlike in the diffusion-limited regime, the surface potential  $\tilde{V}_0$  significantly impacts the phase separation time  $\tau_p$  in a reaction-limited regime, as illustrated in Fig. 5. This is because lower  $\tilde{k}$  values extend the lifetime of smaller chains, making the surface potential more effective due to both the higher mobility and the prolonged lifetime of these smaller molecules. To be more specific, this is attributed to the potential-induced, selective

attraction of  $\phi_A$  to the surface, which allows for faster diffusive transport when the molecular weight is low (*i.e.* at the early stages of phase separation) and leads to an earlier onset of phase separation. As a result, the initial phase separation, driven by the surface potential, intensifies and grows away from the surface in layers. This continues until the average degree of polymerization increases sufficiently through polymerization to further drive phase separation. In essence, the surface potential compensates for the times over which phase separation does not occur due to slower polymerization, resulting in a more pronounced phase separation at smaller  $\tilde{k}$ .





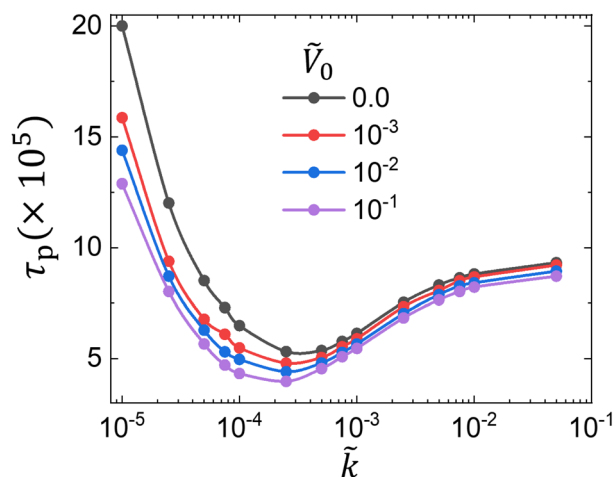


Fig. 5 Phase separation time  $\tau_p$  for various  $\tilde{V}_0$  and  $\tilde{k}$  at constant  $\chi = 1.0$ . We find two different regimes for  $\tau_p$  polymerization-limited and diffusion-limited regimes. As the reaction rate  $\tilde{k}$  initially increases, it shortens phase separation time  $\tau_p$  in a polymerization-limited regime ( $\tilde{k} \leq 10^{-4}$ ). In this regime, increasing  $\tilde{V}_0$  noticeably reduces  $\tau_p$  due to abundant short chains with high mobility. In a diffusion-limited regime ( $\tilde{k} > 10^{-4}$ ), an increase in  $\tilde{k}$  slows down the characteristic phase separation time  $\tau_p$  while the effect of  $\tilde{V}_0$  becomes negligible due to hindered diffusion from rapid accumulation of large polymers.

To characterize the timescales between diffusion and reaction, the Damköhler number  $Da$  is defined:

$$Da = \frac{\tau_{\text{diffusion}}}{\tau_{\text{reaction}}} = \frac{k}{\tilde{v}_0 R_g^3} \frac{N^2 b^2 \zeta_0}{3\pi^2 k_B T} = \frac{\tilde{k} N^2}{C^2 N_0^2}. \quad (11)$$

Here,  $\zeta_0$  is the friction coefficient. At  $\tilde{k} = 10^{-4}$ ,  $Da = 0.15$ , which denotes a reaction-limited regime where polymerization occurs slowly with respect to diffusion and phase separation. In the absence of the surface potential, this leads to longer  $\tau_p$  as the rate  $\tilde{k}$  decreases due to the slow polymerization of chains that must be sufficiently long before phase separation can occur. In Fig. 5, the surface potential drives phase separation for  $\tilde{k} \leq 10^{-4}$ , thus the phase separation process is not limited by the extent of reaction; rather lower  $\tilde{k}$  indirectly helps the process by not rapidly producing heavier polymers which will hinder the phase separation. Conversely, at  $\tilde{k} = 10^{-3}$  or  $Da = 1.5$ , the system is in a diffusion-limited regime ( $\tilde{k} > 10^{-4}$ ) as shown in Fig. 5. In this scenario, the surface potential slightly enhances the phase separation by preferentially attracting molecules but does not make a significant difference due to rapid accumulation of heavier chains from faster polymerization, leading to overall slower dynamics.

We also provide  $\psi(\tilde{t})$  over different rates of reaction at  $\tilde{V}_0 = 10^{-3}$  in Fig. 6a with the corresponding molecular weight distribution  $w_A$  at  $\tilde{t} = 2 \times 10^5$  in Fig. 6b to examine the most abundant species with length  $N_A$  and its behavior at the onset of phase separation. Fig. 6a illustrates how the phase separation parameter  $\psi(\tilde{t})$  varies with the reaction rate  $\tilde{k}$ , contrasting with the dependency on the Flory–Huggins parameter  $\chi$  shown in Fig. 3. At a fixed surface potential  $\tilde{V}_0$ , two distinct trends emerge as previously identified in Fig. 5. Notably, for the

system with  $\tilde{k} = 10^{-5}$ , indicated by the red color in Fig. 6a, phase separation is significantly delayed despite the presence of a surface potential. This delay is attributed to the competition between surface potential and the free energy of polymer mixing, where the surface potential strength ( $\tilde{V}_0 = 10^{-3}$ ) is insufficient to overcome the mixing free energy. Additionally, at this low reaction rate, polymer chains grow very slowly, maintaining miscibility for an extended period. This observation aligns with findings that systems with  $\tilde{V}_0 = 10^{-3}$  behave similarly to zero-potential systems regarding phase separation onset, as depicted in Fig. 3. It is further supported by the slow evolution of molecular weight distribution shown in Fig. 6b. Consistent with our observation, the molecular weight distribution  $w_A$  in Fig. 6b indicates that the smaller chains are abundant for lower  $\tilde{k}$  and the systems accumulate larger chains more as  $\tilde{k}$  increases;  $w_A$  shows which length of polymer is the primary participant in the phase separation process at early time ( $\tilde{t} = 2 \times 10^5$ ). Thus, we attribute an earlier rise of  $\psi(\tilde{t})$  for lower  $\tilde{k}$  to the surface potential which drives the diffusion of unreacted smaller molecules as shown in Fig. 6b, which results in enhanced phase separation as depicted in Fig. 2a, 3 and 5.

We analyze the phase separating regimes away from the surface potential to characterize the “bulk” phase separation regime at  $\tilde{x} = 40$ , where isotropic phase separation (*i.e.*  $\omega(\tilde{x}, \tilde{t}) < 0$ ) occurs as shown in Fig. 4. First, we keep track of  $\omega(\tilde{x}, \tilde{t})$  values over time at  $\tilde{x} = 40$  as shown in Fig. 7 to represent the isotropic phase separation behaviors for the “bulk” regime. In Fig. 7a, we observe that  $\omega(\tilde{x} = 40, \tilde{t})$  curves exhibit a near-collapse for identical  $\tilde{k} > 10^{-4}$  (diffusion-limited regime), irrespective of  $\tilde{V}_0$  values. This behavior is anticipated, given the sufficient distance from the anisotropic concentration wave induced by the surface potential in a diffusion-limited system. The trend closely resembles a system devoid of surface potential, where higher  $\tilde{k}$  values necessitate extended time for phase separation due to the accelerated generation of slower-diffusing, heavier polymers.<sup>94</sup> Consistently, Fig. 7a demonstrates that increasing the reaction rate  $\tilde{k}$  decelerates isotropic bulk phase separation at  $\tilde{x} = 40$ , as illustrated in Fig. 5. Fig. 7b depicts  $\omega(\tilde{x} = 40, \tilde{t})$  for lower reaction rates ( $\tilde{k} \leq 10^{-4}$ ) in the reaction-limited regime, revealing distinct behaviors compared to Fig. 7a. At  $\tilde{k} = 10^{-4}$ , the intensity diminishes significantly, except for  $\tilde{V}_0 = 0$ , relative to Fig. 7a. This reduction signifies the system’s transition from a diffusion-limited to reaction-limited regime, where the surface potential exerts a more pronounced influence on phase separation, as evidenced in Fig. 5. Further reduction of  $\tilde{k}$  to  $10^{-5}$  yields positive values of  $\omega(\tilde{x} = 40, \tilde{t})$ , excluding the zero-potential system. This indicates a deeper penetration of the concentration wave from the surface potential and the development of anisotropic phase separation beyond the point ( $\tilde{x} = 40$ ) previously considered as “bulk”. In this scenario, surface-driven phase separation is sufficient and allows ample time for further propagation, expanding the anisotropic regime while suppressing isotropic phase separation, as demonstrated in Fig. 4e, i, and m.

To more thoroughly understand how different  $\tilde{k}$  values affect the competition between surface-driven and bulk phase separation, we examine volume fractions of each individual chains



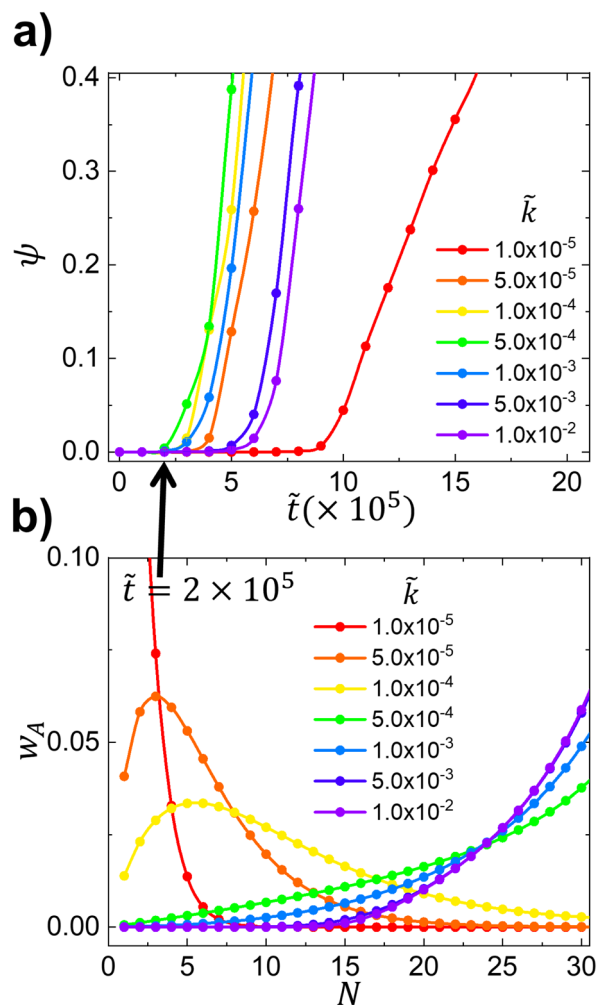


**Fig. 6** (a) The effect of reaction rate  $\tilde{k}$  on  $\psi(\tilde{t})$  at constant  $\tilde{V}_0 = 10^{-3}$  and  $\chi = 1.0$ . (a) shows consistency with previous observations in Fig. 5 that the initial increase in  $\tilde{k}$  leads to faster phase separation but further increase slows down phase separation. (b) shows molecular weight distribution  $w_A$  at  $\tilde{t} = 2 \times 10^5$  in Fig. 6a. It describes the distribution of chain lengths participating in a phase separation process at the moment. This supports the findings that higher  $\tilde{k}$  in a diffusion-hindered regime leads to a longer phase separation time because rapid accumulation of larger chains hinder diffusion and phase separation, and higher  $\tilde{k}$  in a reaction-limited region leads to faster phase separation with increasing polymer incompatibility.

with different degrees of polymerization  $N_A$  for species A. We do not plot species B, which shares the same large- $\tilde{x}$  behavior but exhibits oscillations that are opposite of those in A, and does not provide additional physical insight. We consider both slow ( $\tilde{k} = 10^{-5}$ ) and fast ( $\tilde{k} = 10^{-2}$ ) polymerization kinetics in Fig. 8 and 9, respectively. Fig. 8a provides the overall behavior of  $\omega(\tilde{x}, \tilde{t})$  at a smaller reaction rate ( $\tilde{k} = 10^{-5}$ ) for a reaction-limited regime, which is the same as Fig. 4m. All of the same color in both Fig. 8a and c denotes the same time over the course of phase separation from red ( $\tilde{t} = 0$ ) to purple ( $\tilde{t} = \tau_p$ ) as visualized in Fig. 8b.

In Fig. 8c, the concentration profiles of individual polymer chains with specific chain lengths ( $N_A$ ) along the  $\tilde{x}$ -direction are presented for  $N_A = 1, 2, 4, 8, 16$ , and 32. This analysis examines

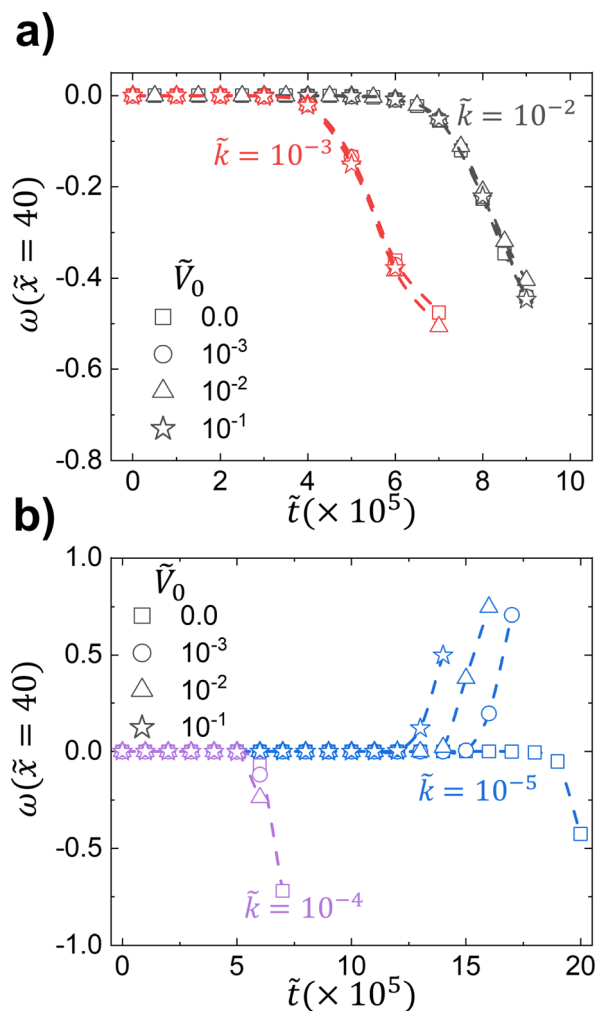


**Fig. 7** The bulk phase separation intensity  $\omega(\tilde{x} = 40, \tilde{t})$  over  $\tilde{k}$  and  $\tilde{V}_0$  at constant  $\chi = 1.0$ . (a) For varying  $\tilde{V}_0$ , the curves nearly collapse onto one another for the same  $\tilde{k}$ . This is expected for a diffusion-limited regime because the anisotropic concentration wave induced by the surface potential propagates less effectively, meaning that phase separation in the “bulk” depends on  $\tilde{k}$ . As the reaction rate  $\tilde{k}$  increases, more time is required for isotropic phase separation in the bulk regime due to the rapid accumulation of longer chains. (b) In a reaction-limited regime, surface potential becomes more dominant due to the prevalent smaller molecules with faster diffusion, effectively altering the bulk phase separation behaviors. At  $\tilde{k} = 10^{-5}$ ,  $\omega(\tilde{x} = 40, \tilde{t})$  shows positive growth for  $\tilde{V}_0 > 0$ , indicating a deeper penetration of anisotropic concentration wave towards the bulk regime as shown in Fig. 4e, i and m.

the role of reaction rate under the influence of surface potential in relation to polydispersity. In the case of a slow reaction rate, monomers ( $N_A = 1$ ) are weakly attracted to the surface potential over time and are continuously consumed through polymerization. For polymers with  $N_A = 2$  and 4, an initial single peak (representing a polymer-rich or concentrated region) forms near the surface potential ( $\tilde{x} = 1$ ), followed by fluctuating concentrations extending toward  $\tilde{x} = 60$  as they are progressively consumed. This behavior persists for larger polymers ( $N_A = 8$ ), with an additional observation of polymer generation during phase separation as the system evolves toward  $\tau_p$ . The



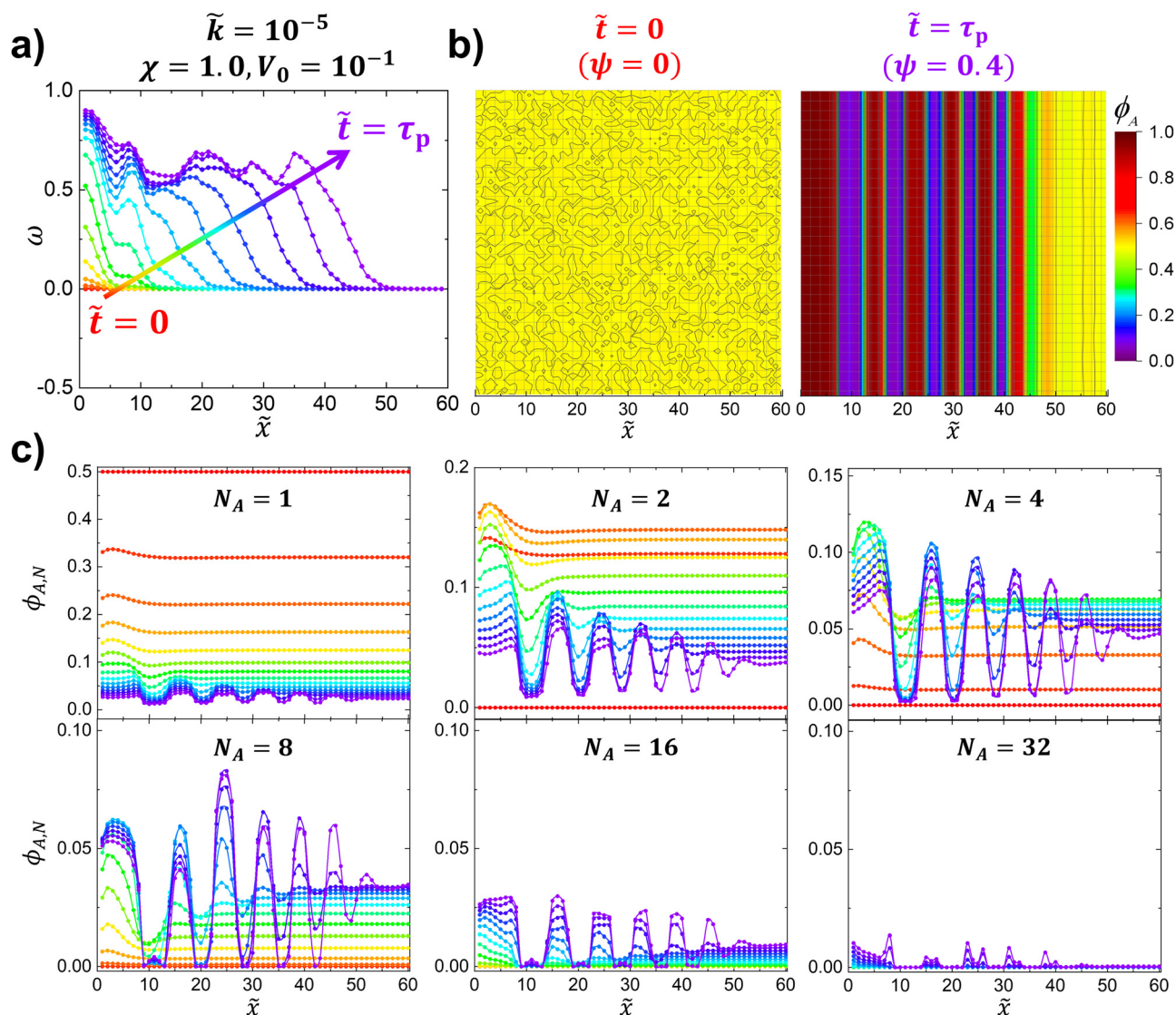


**Fig. 8** Plots demonstrating the dynamic evolution of the full molecular weight distribution for slow polymerization kinetics (*i.e.*  $\tilde{k}$  of  $10^{-5}$ , reaction-limited regime). All figures share the same x-axis for a normalized simulation box, and color scale from red ( $\tilde{t} = 0$ ) to purple ( $\tilde{t} = \tau_p$ ). (a) replicates  $\omega(\tilde{x}, \tilde{t})$  shown in Fig. 4m. (b) The visualization of one of the simulation trajectories at  $\tilde{t} = 0$  and  $\tilde{t} = \tau_p$ . (c) The time-evolution of polymer concentration profiles along  $\tilde{x}$ . Phase separation near the surface potential gets more profound for short- or medium-sized  $N_A$ . Consumption and polymerization are shown with  $N_A = 1, 2$  and  $4$  while generation and polymerization are found with  $N_A = 8, 16$  and  $32$ . In this slower reacting system, smaller molecules diffuse to the surface, accumulate, and polymerize locally, leading to local generation of heavier polymers at the concentrated regions such as near the surface potential.

trend becomes more pronounced with increasing chain length. Heavier polymers ( $N_A = 16$  and  $32$ ) exhibit simultaneous phase separation and generation, suggesting that larger molecules are formed based on the pre-established concentration fields of smaller chains. This eliminates the need for these larger molecules to diffuse and phase separate independently, as smaller molecules have already undergone phase separation over sufficient time at low reaction rates ( $\tilde{k} = 10^{-5}$ ). Fig. 9 instead illustrates a diffusion-limited system with a relatively high polymerization rate constant  $\tilde{k} = 10^{-2}$ , such that short chains are almost immediately consumed by the reaction. All other variables are kept constant as in Fig. 8 to specifically isolate the effect of the polymerization rate. Fig. 9a (which is also shown in Fig. 4p) shows two major differences in terms of

$\omega(\tilde{x}, \tilde{t})$ . First, Fig. 9a exhibits  $\omega(\tilde{x}, \tilde{t})$  values below 0 (*i.e.* isotropic phase separation), which is not observed in Fig. 8a. This is attributed to the comparable timescales between surface-directed phase separation and polymerization-induced phase separation; for  $\tilde{k} = 10^{-2}$ , the system quickly builds up sufficient incompatibility to initiate polymerization-induced phase separation before the surface-driven phase separation becomes dominant. Second, the system exhibits significantly less propagation of anisotropic concentration waves into the bulk, even under the same surface potential strength ( $\tilde{V}_0 = 10^{-1}$ ). This is because smaller molecules are rapidly consumed, limiting their diffusive transport. This rapid consumption turns into the generation of larger molecules with reduced mobility, which hinders overall diffusion in the system even under the surface potential at  $\tilde{k} = 10^{-2}$ .





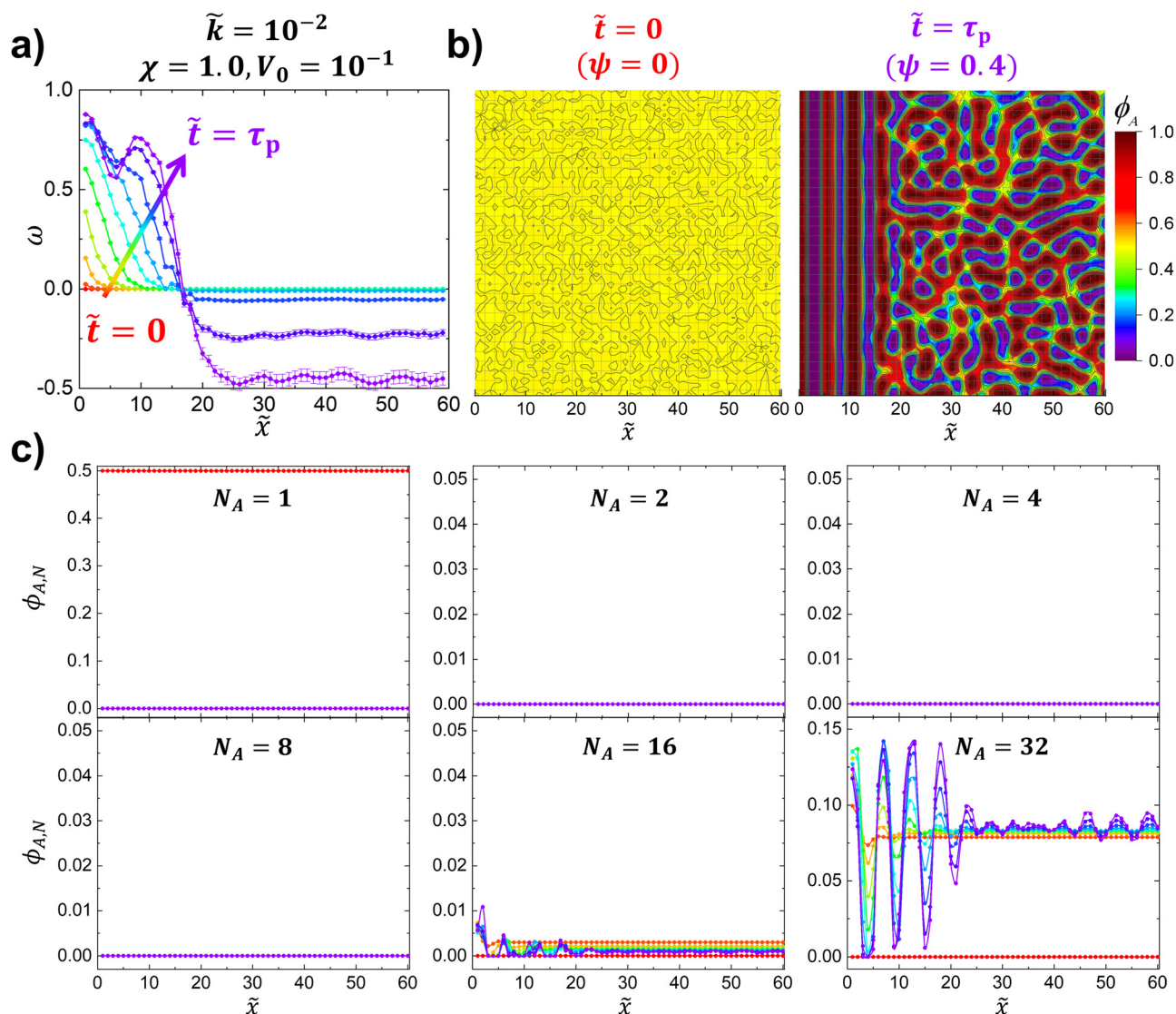


**Fig. 9** Plots demonstrating the dynamic evolution of the full molecular weight distribution for slow polymerization kinetics (i.e.  $\tilde{k}$  of  $10^{-2}$ , diffusion-limited regime). All figures share the same  $x$ -axis for the normalized simulation box, and color scale from red ( $\tilde{t} = 0$ ) to purple ( $\tilde{t} = \tau_p$ ). (a) Replicated  $\omega(\tilde{x}, \tilde{t})$  shown in Fig. 4p. (b) Visualization of one of the simulation trajectories at  $\tilde{t} = 0$  and  $\tau_p$ . (c) The time-evolution of polymer concentration profiles along  $\tilde{x}$ . Phase separation near the surface potential gets more profound for  $N_A = 16$  or  $32$ . No meaningful differences are found but to be completely consumed in  $N_A = 1, 2, 4$  and  $8$  due to large  $\tilde{k}$  of  $10^{-2}$ . For  $N_A = 16$ , mostly consumption takes place while phase separating with small fluctuation near the surface. In  $N_A = 32$ , we observe that it accumulates first before it phase separates. This fast reacting system shows that polymerization is too fast for smaller molecules to diffuse, leading to accumulation of heavier polymers evenly throughout the space first, and then these larger molecules drive the phase separation.

Fig. 9c illustrates that for  $N_A = 1, 2, 4$ , and  $8$ , the reaction (or consumption) rate is so high that molecules have insufficient time to diffuse near the potential surface. Only for larger chain lengths ( $N_A = 16$ ) do we observe subtle simultaneous consumption and phase separation over time. At early times (indicated by red colors), the system exhibits minimal compositional variation and lacks evident phase separation. Gradual phase separation becomes apparent as the system approaches  $\tau_p$ . For the largest chains considered ( $N_A = 32$ ), the system initially shows a nearly uniform accumulation of polymers throughout space due to the rapid reaction rate. This is evident at early times when  $\phi_{A,32}$  averages around  $0.07$  for  $N_A = 32$ , as shown in

Fig. 9c. A concentration wave emerges from the surface potential, propagating into the bulk and driving anisotropic phase separation. Additionally, bulk phase separation occurs at  $\tilde{x} = 40$  over longer timescales near  $\tau_p$ , as depicted in Fig. 9a and b. However, this bulk phase separation does not result in significant changes in  $\phi_{A,32}$  at  $\tilde{x} = 40$  due to spatial averaging along the  $y$ -direction.

## 4 Conclusions

We have modified and developed a pCH model to study how phase separation in a polymerizing binary blend is affected by





the presence of a preferential surface, and show that there is a complex interplay between polymer incompatibility, strength of the preferential surface interactions and polymerization kinetics on the dynamics and structure of the phase separating polymer.

We first demonstrate how the strength  $\tilde{V}_0$  of an applied preferential surface potential affects phase separation (Fig. 2a), and use an order parameter  $\omega(\tilde{x}, \tilde{t})$  (Fig. 2b) and related phase ordering transition quantity  $\tilde{x}_{\omega=0}(\tilde{t})$  (Fig. 2c) to track the phase separation process over time. We found that phase separation at a preferential surface occurs before phase separation in the bulk, because larger values of  $\tilde{V}_0$  locally concentrate one of the species near the surface potential; this increases both the local rate of polymerization and promotes the formation of the phase enriched in the preferred species. This leads to a layered, anisotropic structure at the surface, and we show that this structure grows monotonically with time by monitoring the anisotropic-isotropic transition point  $\tilde{x}_{\omega=0}(\tilde{t})$ . This quantity reveals that stronger  $\tilde{V}_0$  initially results in a thicker anisotropic regime, which repeats contraction upon merging of anisotropic domains and expansion upon further penetration of concentration wave over time.

We further investigate the influence of polymer incompatibility, characterized by  $\chi$ , on the phase separation dynamics in the presence of a surface potential,  $\tilde{V}_0$ . As illustrated in Fig. 3, the behavior of  $\psi(\tilde{t})$  aligns with expectations as  $\chi$  varies; specifically, higher  $\chi$  values result in accelerated phase separation. For each  $\chi$  value, the system exhibits a monotonic dependence on  $\tilde{V}_0$ , where larger  $\tilde{V}_0$  values lead to an earlier onset of the rise in  $\psi(\tilde{t})$ .

We define and employ the order parameter for directional phase separation,  $\omega(\tilde{x}, \tilde{t})$ , across various combinations of the surface potential  $\tilde{V}_0$  and reaction rate  $\tilde{k}$ , as illustrated in Fig. 4. Together with Fig. 5 and the Damköhler number  $Da$  analysis, we identify diffusion-limited and reaction-limited regimes. This framework enables us to systematically explore how phase behavior evolves as a function of  $\tilde{k}$  and  $\tilde{V}_0$  within each regime.

By explicitly accounting for polydispersity in our framework, we investigate the intricate interplay between surface potential and reaction rate, as illustrated by the molecular weight distribution  $w_A$  in Fig. 6b. This analysis provides a clear physical understanding of the dominant factors driving phase separation in both polymerization-limited and diffusion-limited regimes. Furthermore, we explore the spatiotemporal evolution of molecular weight under the influence of surface potential. Our findings reveal distinct phase separation pathways that arise from the competition between the timescales of surface-driven and polymerization-driven phase separation, governed by the polydispersity and molecular weight-dependent mobility.

Overall, we have demonstrated that phase separation under a preferential surface is governed by two distinct processes; surface-driven polymerization and bulk polymerization. The behavior of these two processes is governed by a competition between the polymerization rate and molecular diffusion, which has implications for practical materials systems such as surface-directed<sup>105–108</sup> or self-stratifying<sup>108–110</sup> coatings. This approach could also be further modified to account for other

types of systems, such as coatings involving higher-functionality monomers that can undergo gelation,<sup>111–113</sup> or other types of polymerization reaction kinetics.<sup>113–115</sup> Similarly, it would be possible to modify this approach to account for other polymer dynamic behaviors, in particular directly including entangled polymer dynamics<sup>64,113</sup> through changes to the molecular-weight dependence of the diffusion constant.

## Author contributions

Charles Sing and Hyeonmin Jeong designed the computational model and the theoretical framework, analyzed the data, carried out the implementation, and performed the calculations. Hyeonmin Jeong wrote the manuscript and designed the figures with the supervision of Charles Sing. Junsu Gu, Paul Mwasame, Kshitish Patankar, and Decai Yu provided guidance on the direction of the study. Paul Mwasame and Decai Yu helped connect Dows internal modeling resources. All authors provided critical feedback and helped shape the research and manuscript.

## Data availability

Data for this article, including raw data (\*.xlsx) for all figures and computational code (\*.c) for running the polymerizing Cahn–Hilliard program, are available at <https://github.com/Sing-group-ChBE-UIUC>.

## Conflicts of interest

There are no conflicts to declare.

## Acknowledgements

The authors acknowledge the Dow University Partnership Initiative (UPI Program) for financial support, and also the helpful discussions with Fabio Aguirre-Vargas (Dow), Michael Pacholski (Dow), Harshad Shah (Dow), Guarav Singhal (UIUC), Lihong Lao (UIUC), Piyush Singh (UIUC), Paul Braun (UIUC), Charles Schroeder (UIUC), and Simon Rogers (UIUC). The authors also acknowledge helpful comments from the anonymous reviewers, who found a non-trivial error in our original method.

## References

- 1 R. A. Jones, L. J. Norton, E. J. Kramer, F. S. Bates and P. Wiltzius, *Phys. Rev. Lett.*, 1991, **66**, 1326.
- 2 M. Geoghegan, R. Jones and A. Clough, *J. Chem. Phys.*, 1995, **103**, 2719–2724.
- 3 S. Puri, K. Binder and H. L. Frisch, *Phys. Rev. E: Stat. Phys., Plasmas, Fluids, Relat. Interdiscip. Top.*, 1997, **56**, 6991.
- 4 S. Puri and K. Binder, *Phys. Rev. A: At., Mol., Opt. Phys.*, 1992, **46**, R4487.
- 5 M. Tabatabaieyazdi, P. K. Chan and J. Wu, *Modell. Simul. Mater. Sci. Eng.*, 2015, **23**, 075004.



- 6 S. Ghaffari, P. K. Chan and M. Mehrvar, *Polymers*, 2021, **13**, 256.
- 7 I. C. Henderson and N. Clarke, *Macromol. Theory Simul.*, 2005, **14**, 435–443.
- 8 E. Kim, G. Krausch, E. J. Kramer and J. O. Osby, *Macromolecules*, 1994, **27**, 5927–5929.
- 9 M. Geoghegan, H. Ermer, G. Jüngst, G. Krausch and R. Brenn, *Phys. Rev. E:Stat. Phys., Plasmas, Fluids, Relat. Interdiscip. Top.*, 2000, **62**, 940.
- 10 G. Krausch, E. J. Kramer, F. S. Bates, J. Marko, G. Brown and A. Chakrabarti, *Macromolecules*, 1994, **27**, 6768–6776.
- 11 G. Brown and A. Chakrabarti, *Phys. Rev. A:At., Mol., Opt. Phys.*, 1992, **46**, 4829.
- 12 S. Puri and K. Binder, *J. Stat. Phys.*, 1994, **77**, 145–172.
- 13 S. Puri and K. Binder, *Phys. Rev. Lett.*, 2001, **86**, 1797.
- 14 S. Puri, *J. Phys.: Condens. Matter*, 2005, **17**, R101.
- 15 S. Puri, *Phys. A*, 2007, **384**, 100–107.
- 16 K. Binder, S. K. Das and J. Horbach, *Mod. Phys. Lett. B*, 2009, **23**, 549–565.
- 17 K. Binder, S. Puri, S. K. Das and J. Horbach, *J. Stat. Phys.*, 2010, **138**, 51–84.
- 18 S. Puri, P. Jaiswal and S. K. Das, *Eur. Phys. J.:Spec. Top.*, 2013, **222**, 961–974.
- 19 L.-T. Yan and X.-M. Xie, *Macromol. Theory Simul.*, 2006, **15**, 226–237.
- 20 L.-T. Yan and X.-M. Xie, *Polymer*, 2006, **47**, 6472–6480.
- 21 E. Dickinson and P. Walstra, *Food colloids and polymers: stability and mechanical properties*, Elsevier, 1993.
- 22 T. Russell, *Science*, 2002, **297**, 964–967.
- 23 Y. Vaynzof, D. Kabra, L. Zhao, L. L. Chua, U. Steiner and R. H. Friend, *ACS Nano*, 2011, **5**, 329–336.
- 24 R. A. Jones and R. W. Richards, *Polymers at surfaces and interfaces*, 1999.
- 25 M. Müller and K. Binder, *J. Phys.: Condens. Matter*, 2005, **17**, S333.
- 26 K. Binder, J. Horbach, R. Vink and A. De Virgiliis, *Soft Matter*, 2008, **4**, 1555–1568.
- 27 P.-G. De Gennes, *Rev. Mod. Phys.*, 1985, **57**, 827.
- 28 G. Reiter, *Phys. Rev. Lett.*, 1992, **68**, 75.
- 29 J. Doane, N. Vaz, B.-G. Wu and S. Žumer, *Appl. Phys. Lett.*, 1986, **48**, 269–271.
- 30 R. J. Williams, B. A. Rozenberg and J.-P. Pascault, *Polymer analysis polymer physics*, 2005, pp. 95–156.
- 31 M. A. Hillmyer, P. M. Lipic, D. A. Hajduk, K. Almdal and F. S. Bates, *J. Am. Chem. Soc.*, 1997, **119**, 2749–2750.
- 32 R. Motokawa, Y. Iida, Y. Zhao, T. Hashimoto and S. Koizumi, *Polym. J.*, 2007, **39**, 1312–1318.
- 33 J. Oh and A. Rey, *Comput. Theor. Polym. Sci.*, 2001, **11**, 205–217.
- 34 R. Yu, S. Zheng, X. Li and J. Wang, *Macromolecules*, 2012, **45**, 9155–9168.
- 35 E. S. Zofchak, J. A. LaNasa, V. M. Torres and R. J. Hickey, *Macromolecules*, 2020, **53**, 835–843.
- 36 T. Inoue, *Prog. Polym. Sci.*, 1995, **20**, 119–153.
- 37 F. Meng, S. Zheng, W. Zhang, H. Li and Q. Liang, *Macromolecules*, 2006, **39**, 711–719.
- 38 Z. Dong, H. Cui, H. Zhang, F. Wang, X. Zhan, F. Mayer, B. Nestler, M. Wegener and P. A. Levkin, *Nat. Commun.*, 2021, **12**, 247.
- 39 K. Yamanaka, Y. Takagi and T. Inoue, *Polymer*, 1989, **30**, 1839–1844.
- 40 J. Kim, C. Cho, P. Palfy-Muhoray and T. Kyu, *Phys. Rev. Lett.*, 1993, **71**, 2232.
- 41 L. Peng, J. Cui and S. Li, *Macromol. Chem. Phys.*, 2000, **201**, 699–704.
- 42 J. Zhang, H. Zhang and Y. Yang, *J. Appl. Polym. Sci.*, 1999, **72**, 59–67.
- 43 C. R. Szczepanski, C. S. Pfeifer and J. W. Stansbury, *Polymer*, 2012, **53**, 4694–4701.
- 44 C. R. Szczepanski and J. W. Stansbury, *Polymer*, 2015, **70**, 8–18.
- 45 E. Kemiklioglu and L.-C. Chien, *Eur. Phys. J. E:Soft Matter Biol. Phys.*, 2017, **40**, 1–6.
- 46 G. Liang, S. Yu, Z. Huang, K. Wu, T. Fu, Y. Tang and Z. Li, *Adv. Photonics Res.*, 2021, **2**, 2100185.
- 47 M. W. Schulze, L. D. McIntosh, M. A. Hillmyer and T. P. Lodge, *Nano Lett.*, 2014, **14**, 122–126.
- 48 L. Chen, D. T. Hallinan Jr, Y. A. Elabd and M. A. Hillmyer, *Macromolecules*, 2009, **42**, 6075–6085.
- 49 S. C. Price, X. Ren, A. C. Jackson, Y. Ye, Y. A. Elabd and F. L. Beyer, *Macromolecules*, 2013, **46**, 7332–7340.
- 50 Y. Tang, K. Wu, S. Yu, J. Chen, X. Ding, L. Rao and Z. Li, *Opt. Lett.*, 2020, **45**, 2918–2921.
- 51 D. C. Hoekstra, B. P. van der Lubbe, T. Bus, L. Yang, N. Grossiord, M. G. Debijs and A. P. Schenning, *Angew. Chem.*, 2021, **133**, 11030–11036.
- 52 K. Yamanaka and T. Inoue, *Polymer*, 1989, **30**, 662–667.
- 53 C. B. Bucknall and A. H. Gilbert, *Polymer*, 1989, **30**, 213–217.
- 54 M. Kimoto and K. Mizutani, *J. Mater. Sci.*, 1997, **32**, 2479–2483.
- 55 N. G. Yun, Y. G. Won and S. C. Kim, *Polymer*, 2004, **45**, 6953–6958.
- 56 P. J. Flory, *J. Chem. Phys.*, 1942, **10**, 51–61.
- 57 J. W. Cahn and J. E. Hilliard, *J. Chem. Phys.*, 1958, **28**, 258–267.
- 58 L. Löchte, A. Gitt, G. Gottstein and I. Hurtado, *Acta Mater.*, 2000, **48**, 2969–2984.
- 59 M. Honjo and Y. Saito, *ISIJ Int.*, 2000, **40**, 914–919.
- 60 R. Abazari, H. Rezazadeh, L. Akinyemi and M. Inc, *Comput. Appl. Math.*, 2022, **41**, 389.
- 61 J.-C. Lin and P. Taylor, *Mol. Cryst. Liq. Cryst. Sci. Technol., Sect. A*, 1993, **237**, 25–31.
- 62 N. Vasishtha and E. Nauman, *Chem. Eng. Commun.*, 1994, **129**, 29–39.
- 63 D. Q. He and E. Nauman, *J. Polym. Sci., Part B: Polym. Phys.*, 1997, **35**, 897–907.
- 64 J. Oh and A. D. Rey, *Macromol. Theory Simul.*, 2000, **9**, 641–660.
- 65 A. A. Alfarrarj and E. B. Nauman, *Macromol. Theory Simul.*, 2007, **16**, 627–631.
- 66 P. Inguva, L. R. Mason, I. Pan, M. Hengardi and O. K. Matar, *Data-Centric Eng.*, 2020, **1**, e13.



- 67 S. Dargaville and T. W. Farrell, *Electrochim. Acta*, 2013, **94**, 143–158.
- 68 Y. Zeng and M. Z. Bazant, *MRS Online Proc. Libr.*, 2013, **1542**, 1–15.
- 69 E. B. Nauman and D. Q. He, *Polymer*, 1994, **35**, 2243–2255.
- 70 C. Huang, M. O. de La Cruz and B. Swift, *Macromolecules*, 1995, **28**, 7996–8005.
- 71 B. Barton and A. McHugh, *J. Polym. Sci., Part B: Polym. Phys.*, 1999, **37**, 1449–1460.
- 72 P. Graham, B. Barton and A. McHugh, *J. Polym. Sci., Part B: Polym. Phys.*, 1999, **37**, 1461–1467.
- 73 D. R. Tree, L. F. Dos Santos, C. B. Wilson, T. R. Scott, J. U. Garcia and G. H. Fredrickson, *Soft Matter*, 2019, **15**, 4614–4628.
- 74 K. Luo, *Eur. Polym. J.*, 2006, **42**, 1499–1505.
- 75 K.-W. D. Lee, P. K. Chan and X. Feng, *Macromol. Theory Simul.*, 2003, **12**, 413–424.
- 76 P. K. Inguva, P. J. Walker, H. W. Yew, K. Zhu, A. J. Haslam and O. K. Matar, *Soft Matter*, 2021, **17**, 5645–5665.
- 77 T. Ohnaga, W. Chen and T. Inoue, *Polymer*, 1994, **35**, 3774–3781.
- 78 H. Tanaka, T. Suzuki, T. Hayashi and T. Nishi, *Macromolecules*, 1992, **25**, 4453–4456.
- 79 S. C. Glotzer, E. A. Di Marzio and M. Muthukumar, *Phys. Rev. Lett.*, 1995, **74**, 2034.
- 80 M. D. Tikekar, K. T. Delaney, M. C. Villet, D. R. Tree and G. H. Fredrickson, *Soft Matter*, 2022, **18**, 877–893.
- 81 P. K. Chan and A. D. Rey, *Macromolecules*, 1996, **29**, 8934–8941.
- 82 P. K. Chan and A. D. Rey, *Macromolecules*, 1997, **30**, 2135–2143.
- 83 B. Zhou and A. C. Powell, *J. Membr. Sci.*, 2006, **268**, 150–164.
- 84 F. Boyer, C. Lapuerta, S. Minjeaud, B. Piar and M. Quintard, *Transp. Porous Media*, 2010, **82**, 463–483.
- 85 T. Rogers and R. C. Desai, *Phys. Rev. B: Condens. Matter Mater. Phys.*, 1989, **39**, 11956.
- 86 P.-G. de Gennes, *J. Chem. Phys.*, 1980, **72**, 4756–4763.
- 87 K. Binder, *J. Chem. Phys.*, 1983, **79**, 6387–6409.
- 88 C. Huang and M. Olvera de La Cruz, *Macromolecules*, 1994, **27**, 4231–4241.
- 89 E. D. Siggia, *Phys. Rev. A: At., Mol., Opt. Phys.*, 1979, **20**, 595.
- 90 A. J. Bray, *Adv. Phys.*, 2002, **51**, 481–587.
- 91 P. C. Hohenberg and B. I. Halperin, *Rev. Mod. Phys.*, 1977, **49**, 435.
- 92 W. Chen, C. Wang, X. Wang and S. M. Wise, *J. Comput. Phys.*, 2019, **3**, 100031.
- 93 P.-H. Chiu, *J. Comput. Phys.*, 2019, **392**, 115–140.
- 94 H. Jeong, J. Gu, P. Mwasame, K. Patankar, D. Yu and C. E. Sing, *Soft Matter*, 2024, **20**, 681–692.
- 95 G. Odian, *Principles of polymerization*, John Wiley & Sons, 2004.
- 96 P. K. Inguva, P. J. Walker, H. W. Yew, K. Zhu, A. J. Haslam and O. K. Matar, *Soft Matter*, 2021, **17**, 5645–5665.
- 97 H. Tang and K. F. Freed, *Macromolecules*, 1991, **24**, 958–966.
- 98 D. Prusty, V. Pryamitsyn and M. Olvera de la Cruz, *Macromolecules*, 2018, **51**, 5918–5932.
- 99 A. Z. Akcasu, *Macromolecules*, 1989, **22**, 3682–3689.
- 100 J. T. Cabral and J. S. Higgins, *Prog. Polym. Sci.*, 2018, **81**, 1–21.
- 101 G. R. Strobl, *Macromolecules*, 1985, **18**, 558–563.
- 102 H. Tang and K. F. Freed, *J. Chem. Phys.*, 1991, **94**, 6307–6322.
- 103 R. Alhasan and D. R. Tree, *Macromolecules*, 2022, **55**, 759–765.
- 104 P. J. Steinhardt, D. R. Nelson and M. Ronchetti, *Phys. Rev. B: Condens. Matter Mater. Phys.*, 1983, **28**, 784.
- 105 H.-G. Braun and E. Meyer, *Thin Solid Films*, 1999, **345**, 222–228.
- 106 I. Povstugar, P.-P. Choi, D. Tytko, J.-P. Ahn and D. Raabe, *Acta Mater.*, 2013, **61**, 7534–7542.
- 107 J. Rysz, H. Ermer, A. Budkowski, M. Lekka, A. Bernasik, S. Wrobel, R. Brenn, J. Lekki and J. Jedlinski, *Vacuum*, 1999, **54**, 303–307.
- 108 A. Budkowski, A. Bernasik, P. Cyganik, J. Rysz and R. Brenn, *e-Polymers*, 2002, **2**, 005.
- 109 J. Baghdachi, H. Perez, P. Talapatcharoenkit and B. Wang, *Prog. Org. Coat.*, 2015, **78**, 464–473.
- 110 S. Zahedi and S. Ghaffarian, *Trans. IMF*, 2021, **99**, 133–140.
- 111 Z. Mester, A. Mohan and G. H. Fredrickson, *Macromolecules*, 2011, **44**, 9411–9423.
- 112 J. Ambati and S. E. Rankin, *J. Colloid Interface Sci.*, 2011, **362**, 345–353.
- 113 S. P. Danielsen, A. N. Semenov and M. Rubinstein, *Macromolecules*, 2023, **56**, 5661–5677.
- 114 Q. Tran-Cong-Miyata and H. Nakanishi, *Polym. Int.*, 2017, **66**, 213–222.
- 115 H. Nakanishi, M. Satoh, T. Norisuye and Q. Tran-Cong-Miyata, *Macromolecules*, 2006, **39**, 9456–9466.

